Astronomy & Astrophysics manuscript no. paper
October 14, 2014
© ESO 2014

The evolution of a binary in a retrograde circular orbit embedded in an accretion disk

P.B. Ivanov[1,2], J. C. B. Papaloizou[2], S.-J. Paardekooper[3], and A.G. Polnarev[3]

[1] Astro Space Centre, P. N. Lebedev Physical Institute, 84/32 Profsoyuznaya st., Moscow, 117997, Russia

[2] DAMTP, University of Cambridge, Wilberforce Road, Cambridge CB3 0WA, UK

[3] Astronomy Unit, Queen Mary University of London, Mile end Road, London, E1 4NS, UK

e-mail: pbi20@cam.ac.uk

Draft Version October 14, 2014

arXiv:1410.3250v1 [astro-ph.HE] 13 Oct 2014

ABSTRACT

Aims. Supermassive black hole binaries may form as a consequence of galaxy mergers. Both prograde and retrograde orbits have been proposed. We study a binary of a small mass ratio, q, in a retrograde orbit immersed in and interacting with a gaseous accretion disk in order to estimate time scales for inward migration leading to coalescence and the accretion rate to the secondary component.
Methods. We employ both semi-analytic methods and two dimensional numerical simulations, focusing on the case where the binary mass ratio is small but large enough to significantly perturb the disk.
Results. We develop the theory of type I migration for this case and determine conditions for gap formation finding that then inward migration occurs on a time scale equal to the time required for one half of the secondary mass to be accreted through the unperturbed disk, with accretion onto the secondary playing only a minor role. The semi-analytic and fully numerical approaches are in good agreement, the former being applicable over long time scales.
Conclusions. Inward migration induced by interaction with the disk alleviates the final parsec problem. Accretion onto the secondary does not significantly affect the orbital evolution, but may have observational consequences for high accretion efficiency. The binary may then appear as two sources of radiation rotating around each other. This study should be extended to consider orbits with significant eccentricity and the effects of gravitational radiation at small length scales. Note too that torques acting between a circumbinary disk and a retrograde binary orbit may cause the mutual inclination to increase on a timescale that can be similar to, or smaller than that for orbital evolution, depending on detailed parameters. This is also an aspect for future study.

Key words. Accretion disks: -binaries, Hydrodynamics, Galaxies: quasars: supermassive black holes, Planet-disk interactions

1. Introduction

The merger of two galaxies could lead to the formation of a supermassive binary black hole (SBBH) in the centre of the newly formed more massive galaxy as a result of dynamical friction, (see e.g. Komberg 1968, Begelman, Blanford & Rees 1980). The coalescence of supermassive black holes results in a burst of gravitational radiation, which can in principle be detected by planned space based gravitational antennae, when originating from cosmological distances, (see e.g. Grishchuk et al. 2001; Amaro-Seoane et al. 2013).

The orbit of SBBH shrinks towards coalescence as a result of the operation of a number of mechanisms. These include; frictional interaction with a gaseous component that may reside in the form of an accretion disk, gravitational interaction with the stars of a central star cluster, and the emission of gravitational waves. It was noted by Begelman, Blanford & Rees (1980) that orbital evolution of the SBBH induced by gravitational radiation and gravitational interaction with a star cluster may not be efficient at intermediate scales of order of $0.01 - 1pc$ so that it may stall when its semi-major axis reaches these scales. This has been called the final parsec problem.

This problem may be alleviated by taking into account the interaction with a gaseous component of the system assumed to be in the form of a circumbinary accretion disk, see e.g. Ivanov, Papaloizou & Polnarev (1999), hereafter IPP, Gould & Rix (2000), and more recently e.g Cuadra et al. (2009), Haiman, Kocsis & Menou (2009), Lodato et at (2009), Rossi et al. (2010), Farris et al. (2011), Roedig et al. (2012), Kocsis, Haiman & Loeb (2012), Tanaka, Menou & Haiman (2012), Hayasaki, Saito & Mineshige (2013), Rafikov (2013) and Gold et al. (2013) and references therein. Apart from providing a possible solution to the final parsec problem, the time variability of the accretion rate supplied by an accretion disk around a SBBH, peculiarities in emission spectra, etc. may serve to indicate its presence (e.g. Rieger & Mannheim 2000; Yu & Lu 2001; Armitage & Natarajan 2002, Liu 2004; Lobanov & Roland 2005; Komossa 2006; McFadyen & Milosavljevic 2008; Bogdanovic et al. 2008, 2009; Montuori et al. 2011, 2012; Sesana et al. 2012; Valtonen, Ciprini & Lehto 2012; Burke-Spolaor 2013; Ju et al. 2013; Farris et al. 2014;

McKernan et al. 2014; Roedig et al., 2014 and references therein). In addition, the filling of the central regions of the accretion disk after SBBH coalescence under various circumstances, may also provide indirect observational evidence that the event of SBBH coalescence actually takes place (see e.g. Loeb 2007; Shapiro 2010).

It has been commonly assumed that the direction of motion of the disk gas and the orbital motion of the SBBH coincide. However, as noted by Nixon, King & Pringle (2011) and Nixon et al. (2011), this may not always be the case. Since the direction of the binary orbital motion may not be correlated with the initial direction of the gas motion within the disk. For example the system considered may correspond to the inner regions of a disk galaxy which on large scales consists of counter rotating gas and stars (see e.g. Corsini 2014 for a review) with the gas containing a relatively small part of the total angular momentum content. In that case gas starting with extreme orbital inclination relative to the stellar component is naturally expected to settle into a counter rotating state (e.g. Thakar & Ryden 1998).

Thus the SBBH may be aligned with orbital motion being either prograde or retrograde with respect to the direction of orbital motion of the disk gas. This can be understood as follows. Let us consider a SBBH consisting of a primary with mass M and a secondary with mass M_p, and assume, for simplicity, that the mass ratio q is small, $q \ll 1$. We assume that there is an inclined thin circumbinary accretion disk with a typical mass, M_d, within the scale of the SBBH semi-major axis, a, which is much smaller than M_p. At distances much larger than a the gravitational field of SBBH may be approximated by it's time average form, namely the gravitational field due to a ring of mass M_p and radius a. It was shown by IPP that the disk must align into the binary plane on a scale larger than a. Clearly, when the mass of the secondary greatly exceeds the disk mass on this alignment scale, and as here only the time averaged potential of the binary matters, the direction of alignment will not depend on the direction of SBBH binary motion, and the disk may align with either prograde or retrograde orbital motion, depending on which of these requires the inclination change of least magnitude (see King et al. 2005) [1]. In this paper we shall assume that the configuration of the system and source of disk gas enables retrograde binary orbital motion with respect to the disk to be set up. Note, however, that after the initial alignment process, gravitational torques exerted between a twisted circumbinary disk and a slightly misaligned binary orbit, through which there is an accretion flow, may tend to overturn the orbital plane of the binary on a long time scale when there is counter-rotation (see e.g. Scheuer & Feiler 1996; IPP; King et al. 2005; Nixon, King & Pringle 2011). The timescale associated with this process is determined by the magnitude of the gravitational torque exerted by the twisted accretion disk on the binary. In the linear regime of small mutual inclinations, this torque can be quite large when the effective Shakura-Sunyaev α parameter (Shakura & Sunyaev 1973) governing the evolution of the twisted disk is small. However, once the inclination of the disk with respect to the orbital plane at large distances is significant, non-linear effects come into play and are expected to reduce the value of the torque (see e.g. Ogilvie 1999). In this situation we estimate the timescale of the evolution of binary orbital plane assuming that the effective $\alpha \sim 1$ as was done in IPP (see their equation (23)). We discuss this estimate further in section 12.3 showing that the time scale is expected to be comparable to or even slightly smaller than the timescale of evolution of the binary semi-major axis, depending on the disk parameters and binary mass ratio. Thus, depending on these, the binary may be expected to evolve in the state of retrograde rotation for long enough to undergo significant changes to its orbit and in some cases the effect of secular changes of its orientation may become important. However, for simplicity, in what follows we neglect this possibility, assuming that the planes of the binary and the disk are aligned.

The evolution of a SBBH immersed in the accretion disk and rotating in the retrograde sense has recently been explored numerically using the SPH method for a relatively large mass ratio $q \geq 0.1$ (see e.g. Roedig & Sesana 2014). In addition McKernan at al. (2014) have recently considered the opposite limit of an extremely small mass ratio $q = 10^{-4}$ using the grid based PENCIL CODE.

In this Paper we present a simple semi-analytic theory of a retrograde binary, with mass ratio in the range we consider, immersed in and interacting with a thin accretion disk together with the results of two dimensional numerical hydrodynamical simulations of representative systems. Unlike the works mentioned above, we consider the case when the mass ratio $q \leq 2 \cdot 10^{-2}$ is small but still large enough to significantly affect the evolution of the disk surface density. We consider both disks of formally infinite extent and disks with a finite outer boundary with various prescriptions for the effective viscosity. As two dimensional numerical simulations become problematic for disks with a large dynamic range that are likely to be relevant for SBBH, we develop a simpler applicable one dimensional approach validating through making comparisons with the two dimensional simulations. For this first treatment we focus on the simplest case of a binary with a circular orbit interacting only with the disk while briefly discussing features that should be tackled in future work such as orbital eccentricity and orbital evolution induced by gravitational radiation.

The plan of this Paper is as follows. We give the basic definitions and set-up in section 2 and go on to describe a framework for a one dimensional model for calculating the evolution of the disk and binary orbit in section 3. In this model, the evolution of the disk surface density is governed by a diffusion equation that incorporates a simple model of the angular momentum exchange between the perturber and disk through gravitational scattering. For small mass ratios the perturber remains embedded in the disk, producing a linear response that induces type I migration. The theory of this is presented in section 4 and expressions for the migration rate given. A comparison with migration rates obtained from two dimensional numerical simulations is then undertaken in section 5. The two approaches are found to be in good agreement. Angular momentum exchange with the disk is expected to result in gap formation for sufficiently massive perturbers. This process is studied in section 6 using the one dimensional model set up in section 2. Gap formation was determined to occur for perturber mass ratios exceeding an estimated value $\sim 1.57\delta^2$, with δ being the disk aspect ratio. Simple 1D modelling

[1] Hydrodynamic interaction of the secondary with the accretion disk during the alignment process is discussed in e.g. Ivanov, Igumenshchev & Novikov (1998).

of the gap surface density profile for the case of relatively large mass ratio is described in section 7.

As two dimensional simulations are time consuming and impractical for disks with a very large dynamic range, we go on to develop the more applicable simple one dimensional model in section 8. This is later validated it by making additional detailed comparisons between the two approaches. In the one dimensional model one can calculate the evolution of the disk surface density in the first instance assuming the radius of the assumed circular orbit is a fixed parameter. One can then use this solution to determine how the orbit evolves. It turns out that when a deep gap is formed only the disk exterior to the perturber has to be considered as is explained in section 8.1. A relevant similarity solution for an accretion disk of infinite extent is given in 8.2. and the time scale for orbital evolution induced through the action of disk torques discussed in section 9. In addition accretion rate onto the perturber is estimated in section 10.

We compare the results of the one dimensional model regarding gap formation and migration for larger mass perturbers, with two dimensional numerical simulations in section 11. The two approaches are again found to be in good agreement.

We go on to briefly discuss additional features that should be considered in future work, such as possible effects of a moderate to large imposed orbital eccentricity, orbital evolution driven by the emission of gravitational waves, a process that may dominate when the perturber reaches the inner regions of the disk, and the secular evolution of the direction of binary's angular momentum due to interaction with a twisted accretion disk, in section 12. Finally we summarise our results and conclusions in section 13

2. Basic definitions and set-up

We consider a binary consisting of a primary of mass M and a secondary of mass M_p that is embedded in an accretion disk. The binary orbit is taken to be coplanar with the disk mid-plane, approximately circular and with a sense of rotation that is opposite to that of the disk gas. We suppose that that the primary is much more massive than the secondary such that the mass ratio $q = M_p/M \ll 1$. Thus disk material interior to the orbit of the secondary revolves approximately in circles centred on the primary.

We determine the modification of the disk structure due to the presence of the binary and the evolution of the binary separation distance, r_p, induced by torques exerted by the disk material. In order to do this we employ a simple numerical approach based on an azimuthally averaged and hence simplified one dimensional description of the accretion disk as well as an additional simplified analytic treatment of the problem. We go on to relate these to two-dimensional numerical simulations of the disk interaction with the binary. In the work presented below, we adopt a cylindrical coordinate system (r, ϕ, z) with origin at the primary and with the z axis directed perpendicular to the orbital plane. We assume that the disk material and the binary orbit with increasing and decreasing azimuthal angle and thus in a prograde and retrograde sense respectively.

3. A one dimensional model for the evolution of the disk and binary orbit

We develop a simplified one dimensional model for the evolution of the binary orbit taking into account the gravitational interaction with the disk (e.g. Lin & Papaloizou 1986) which itself undergoes viscous evolution due to angular momentum transport (e.g. Lynden-Bell & Pringle 1974).

3.1. The evolution of the accretion disk and its interaction with the binary orbit

In order to find the torque T due to the disk acting on the binary it is necessary to determine how the presence of the perturbing body affects the structure of the disk. Following the discussion of Lin & Papaloizou (1986) applicable to the case when the binary and disk rotate in the same sense, we assume that the gravitational interaction results in a locally induced angular momentum transport to the disk. This in turn, together with internal angular momentum transport induced by the action of an effective turbulent viscosity, determines the evolution of the disk surface density Σ.

The evolution of Σ can be obtained from consideration of the conservation of mass and angular momentum. The former is expressed by the continuity equation which can be written as

$$\frac{\partial \Sigma}{\partial t} = \frac{1}{2\pi r}\frac{\partial \dot{M}}{\partial r}, \tag{1}$$

where the mass flux through radius r is given by

$$\dot{M} = -2\pi \Sigma r v_r, \tag{2}$$

with v_r being the radial velocity of the disk material.

The conservation of the z-component of angular momentum is expressed by the equation

$$r^2\Omega\frac{\partial \Sigma}{\partial t} = \frac{1}{2\pi r}\frac{\partial \dot{L}}{\partial r} + \Sigma \dot{J}, \tag{3}$$

where the angular momentum flux through radius r is given by

$$\dot{L} = 2\pi\left(\nu r^3 \Sigma \frac{d\Omega}{dr} - \Sigma r^3 \Omega v_r\right), \tag{4}$$

with ν being the kinematic viscosity of the disk material, $\Omega(r) = \sqrt{GM/r^3}$ is its angular velocity which is assumed to be Keplerian and G is the gravitational constant. The torque exerted per unit mass by the perturber on the disk is $\dot{J}$. Thus the total torque exerted on the disk by the perturber is given by

$$T = 2\pi \int r dr \Sigma \dot{J}. \tag{5}$$

Note that unlike the prograde case there are no Lindblad resonances in the retrograde circular case, and, accordingly, their contribution is not included in (5). However, they can operate when a retrograde binary has some eccentricity. This effect is briefly discussed in section 12.1 below.

3.2. The evolution of the binary orbit

By Newton's third law, the total torque exerted on the binary will be $-T$. Provided that it remains approximately

circular, angular momentum conservation for the orbit determines the evolution of r_p through

$$\dot{L}_b = -T, \quad \text{with} \quad L_b = -qM\sqrt{GMr_p}, \tag{6}$$

being the orbital angular momentum, which has a negative sign on account of the orbit being retrograde. From equation (6) we find

$$\dot{r}_p = -\frac{r_p}{t_{ev}} \quad t_{ev} = \frac{|L_b|}{2|T|}. \tag{7}$$

which defines a characteristic timescale, t_{ev}, for the orbital evolution.

Note that for the configuration considered here, the binary is expected to transfer retrograde angular momentum to the disk causing it to slowly spiral inwards. Thus we expect $\dot{J} \leq 0$ and $T \leq 0$. As a consequence the disk will gain retrograde, or equivalently lose prograde, angular momentum. Note that we expect $\dot{J} \leq 0$ everywhere. Thus unlike the case for which the binary is prograde, $\dot{J}$ does not change sign on crossing the orbit.

We now go consider two regimes of perturber disk interaction. The first, appropriate for small mass ratios, is when the disk surface density is only slightly modified such that the interaction can be regarded as linear. It corresponds to the Type I migration regime. The second, appropriate for large enough mass ratios, is when the interaction is nonlinear such that a gap is formed in the disk. In this case, corresponding to Type II migration, migration rates become significantly reduced relative to the Type I regime.

4. Small mass ratios and type I migration

In this case we assume that the perturber has a small enough mass such that the disk surface density remains unchanged by the embedded perturber, at least on long enough time scales such that significant migration can occur. In this regime, the torque exerted on the perturber through interaction with the disk occurs through the excitation, transport and dissipation of density waves. In order to find the resulting torque, T_{wave}, exerted on the binary we perform a linear calculation of the disk response. This approach is standard when considering the type I migration regime in the prograde case (see e.g. Baruteau et al. 2014).

We begin by performing a Fourier expansion of the gravitational potential of the perturber, ψ_p, in the form

$$\begin{aligned}
\psi_p &= \mathcal{R}e \sum_{m=0}^{\infty} W_m \exp[\mathrm{i}m(\varphi + \omega t)] \quad \text{with} \\
W_m &= -\frac{GM_p}{\pi} \int_0^{2\pi} \frac{\cos m\varphi d\varphi}{\sqrt{r_p^2 + r^2 + \Delta_s^2 - 2rr_p\cos\varphi}} \\
&\sim -\frac{2GM_p}{\pi r_p} K_0\left(\frac{m\sqrt{\Delta^2+\Delta_s^2}}{r_p}\right) \quad \text{for} \;\; m > 0.
\end{aligned} \tag{8}$$

Here m is the azimuthal mode number we recall that $\Delta = |r - r_p|$, $\omega = \sqrt{GM/r_p^3}$ is the binary orbital frequency and K_0 denotes the modified Bessel function of the second kind. A gravitational softening length, Δ_s, is included. This is regularly used to approximately account for 3D effects (e.g. Baruteau et al. 2014). The representation of the Fourier coefficient through a Bessel function, as well as the neglect of the indirect term in the perturbing potential, should be accurate either for small $\Delta_{eff} = \sqrt{\Delta^2 + \Delta_s^2}/r_p$ or for $m\Delta_{eff}$ up to of order unity in the limit of large m. We shall assume that one of these conditions is appropriate from now on.

For a barotropic equation of state, the disk response to the action of the perturbing potential (8) can be obtained from equations (45) and (46) of Lin & Papaloizou (1993) with forcing frequency applicable to a secondary in a retrograde circular orbit. These take the form

$$\begin{aligned}
&\frac{1}{\Sigma r}\frac{d\left(\Sigma r \xi_{r,m}\right)}{dr} - \frac{2\Omega\xi_{r,m}}{r(\Omega+\omega)} = \\
&K_m\left(\frac{1}{r^2(\Omega+\omega)^2} - \frac{1}{c^2}\right) + \frac{W_m}{r^2(\Omega+\omega)^2}.
\end{aligned} \tag{9}$$

and

$$\begin{aligned}
&\frac{dK_m}{dr} + \frac{2\Omega K_m}{r(\Omega+\omega)} = \\
&\left[m^2(\Omega+\omega)^2 - \Omega^2\right]\xi_{r,m} - \frac{dW_m}{dr} - \frac{2\Omega W_m}{r(\Omega+\omega)}.
\end{aligned} \tag{10}$$

Here $\xi_{r,m}$ and K_m are the Fourier coefficients in the expansions analogous to (8) for the radial component of the Lagrangian displacement and $W = \Sigma' c^2/\Sigma$ respectively, with Σ' being the induced surface density perturbation. The local sound speed is c.

Local approximation

As the typical wavelength of the density wave response is $\sim c/(m\omega) \ll r$ even for $m = 1$ we expect that they attain the form of outgoing waves for $|r - r_p|/r_p \ll 1$. Thus it is appropriate to look for local solutions for which outgoing wave boundary conditions are applied at radii close to the orbital radius of the perturber.

We thus assume Σ and c^2 are constant and replace r and Ω where they appear explicitly by r_p and ω respectively. As $c^2 \ll r^2\omega^2$, the second term on the LHS and first term on the RHS of equation (9) are neglected. This then becomes

$$\frac{d\xi_{r,m}}{dr} = -\frac{K_m}{c^2} + \frac{W_m}{4r^2\omega^2} \tag{11}$$

and using the same approximation scheme (10) becomes

$$\frac{dK_m}{dr} = (4m^2-1)\omega^2\xi_{r,m} - \frac{dW_m}{dr} - \frac{W_m}{r}. \tag{12}$$

We now use (11) to eliminate K_m in (12) noting that in our approximation scheme it turns out that the second term on the RHS of (11) may be neglected. We thus obtain a governing equation for $\xi_{r,m}$ of the form

$$c^2\frac{d^2\xi_{r,m}}{dr^2} = -(4m^2-1)\omega^2\xi_{r,m} + \frac{dW_m}{dr} + \frac{W_m}{r}. \tag{13}$$

This is seen to be an equation for a forced simple harmonic oscillator. However, it is important to note that, through its dependence on the gravitational potential of the perturber, the effective forcing term involving W varies rapidly in its vicinity and cannot be assumed to be constant. It is convenient to write the governing equation in the compact form

$$\frac{d^2\xi_{r,m}}{dr^2} = -k^2\xi_{r,m} + S, \tag{14}$$

where $k^2 = (4m^2 - 1)\omega^2/c^2$ and
$S = \left(dW_m/dr + W_m/r_p \right) / c^2$.

Solution of the governing equation for the linear response

Equation (14) is solved subject to radiation boundary conditions. For convenience we adopt the convention that ω and k are positive. The free solutions of (14) corresponding to inward and outward propagating density waves are then

$$\begin{aligned} \xi_{r,m} &= C_1 \exp(\mathrm{i}kx) \quad \text{and} \\ \xi_{r,m} &= C_2 \exp(-\mathrm{i}kx), \end{aligned} \tag{15}$$

where $x = r - r_p$ and C_1 and C_2 are arbitrary constant amplitude factors respectively and real parts are taken to obtain physical solutions here and below when needed. The solution to the forced problem is determined such that it takes a multiple of the above forms at large distances (measured in terms of wavelengths) interior to and exterior to the source, respectively.

The required solution is found by standard methods to be given by

$$\xi_{r,m} = \frac{\mathrm{i}}{2k} \int_{-\infty}^{\infty} \exp(-\mathrm{i}k|x - x'|) S(x') dx', \tag{16}$$

with the constants C_1 and C_2 which specify the amplitude of the inward and outward propagating waves at large distances being readily seen to be given by

$$\begin{aligned} C_1 &= \frac{\mathrm{i}}{2k} \int_{-\infty}^{\infty} \exp(-\mathrm{i}kx') S(x') dx' \quad \text{and} \\ C_2 &= \frac{\mathrm{i}}{2k} \int_{-\infty}^{\infty} \exp(\mathrm{i}kx') S(x') dx'. \end{aligned} \tag{17}$$

Rate of angular momentum transport

Each of the waves described above transfers angular momentum from the orbit to the disk at the locations where they eventually dissipate. In a low viscosity disk, dissipation occurs as a result of non linear steepening and shock formation. Depending on their amplitudes, this may be some distance away from the location of the orbit. As the orbit is retrograde with respect to the disk, the transfer removes positive angular momentum from the disk, potentially causing it to accrete onto the central object. The rate of flow of angular momentum through a circle of radius, r, associated with either of the waves is

$$F_J = -\mathcal{I}m \left(\pi m c^2 r_p \Sigma \xi_{r,m} \frac{d\xi^*_{r,m}}{dr} \right), \tag{18}$$

where $\mathcal{I}m$ denotes that the imaginary part is to be taken. We evaluate this expression for ingoing and outgoing waves with a particular value of m. These both remove negative angular momentum from the binary orbit and ultimately transfer it to the disk, accordingly giving additive contributions to the torque acting on the disk which we write as $-T_{wave}$. The corresponding torque acting on the perturber will then be T_{wave}, which is positive. On account of it being retrograde, this acts so as to make the perturber spiral inwards. For a particular value of m, we thus obtain

$$T_{wave} = \pi m c^2 k r_p \Sigma (|C_1|^2 + |C_2|^2). \tag{19}$$

This quantity is directly related to the Fourier transform of the source, $S(x)$, through equation (17). A useful result that enables its evaluation is provided by the standard integral

$$\int_{-\infty}^{\infty} \exp(\mathrm{i}kx) K_0 \left(\frac{m\sqrt{x^2 + \Delta_s^2}}{r_p} \right) dx = \frac{\pi}{\sqrt{k^2 + m^2/r_p^2}} \exp\left(-\Delta_s \sqrt{k^2 + m^2/r_p^2} \right). \tag{20}$$

Making use of (17) and (20), from equation (19) we find that

$$T_{wave} = \frac{2\pi \Sigma G^2 M_p^2 (1 + k^2 r_p^2)}{m r_p k c^2 (1 + k^2 r_p^2/m^2)} \exp\left(-2\Delta_s \sqrt{k^2 + m^2/r_p^2} \right). \tag{21}$$

As $k >> m/r_p$ for all $m \geq 1$, we simplify (21) to read

$$T_{wave} = \frac{2\pi m \Sigma r_p^4}{\sqrt{4m^2 - 1}} q^2 \delta^{-1} \omega^2 \exp\left(-2\Delta_s \sqrt{4m^2 - 1}/H \right) \tag{22}$$

and we recall that $q = M_p/M$ and $\delta = H/r$. This shows that when $\Delta_s \sim H$, as is expected to be appropriate for approximately accounting for the finite disk thickness and as adopted in many of our numerical simulations, the dominant contributions come from the smallest m. This is unlike the prograde case for which the dominant contributions come from $m \sim r_p/H$. Taking into account only $m = 1$, we calculate a migration time for the perturber using (7) with $|T| = |T_{wave}|$, thus obtaining

$$\frac{-\dot{r}_p}{r_p} = \frac{1}{t_{ev}} = \frac{4\pi \Sigma r_p^2}{\sqrt{3}} \left(\frac{r_p}{H} \right) \frac{M_p}{M^2} \omega \exp\left(-2\sqrt{3}\Delta_s/H \right). \tag{23}$$

Comparing this expression with the corresponding one given by Tanaka et al. (2002) for the prograde case and a uniform surface density, we find that t_{mig} is slower by a factor

$$\frac{2.7\sqrt{3}}{4\pi} \left(\frac{r_p}{H} \right) \exp\left(2\sqrt{3}\Delta_s/H \right) \sim 59$$

for the parameters of two dimensional simulations we performed to test (23).

4.1. Total torques obtained by summing over m

When a sum of the contributions from all values of m is performed, the analytic theory indicates that total torque should be $\propto \Delta_s^{-1}$ as the softening length tends to zero. However, our derivation of the expression (22) relies on the assumption that the linear theory is valid. Clearly, this falls when a typical inverse wavenumber associated with the disk response, $k^{-1} \sim \delta r_p/(2m)$, becomes comparable to or less than the accretion radius $r_a \sim q r_p/2$ (this defines the impact parameter for significant scattering if the response were purely ballistic). Using the equality $r_a = k^{-1}$ to define a maximal cutoff value of m, m_{max}, we obtain $m_{max} \sim \delta/q$. Summing contributions from different values of m given by (22) up to this cut off, we obtain an estimate of the total torque corresponding to the low mass retrograde case as

$$T^r_{wave} = \sum_{m=1}^{m_{max}} T_{wave} \sim \pi q \Sigma \omega^2 r_p^4. \tag{24}$$

4.2. Type I migration rates

We remark that (24) gives the migration torque with the cut off scale assumed to be governed by the accretion radius. However, if the accretion radius is less than the scale height the cut off is more likely to be determined by the latter. To deal with that case we replace r_a by $0.3\pi H$ in the above determination of m_{max}. To take account of both possibilities, we multiply the torque given by (24) by a factor f, where $f = min(1, 5q/(3\pi\delta))$. Thus

$$T^r_{wave} = \pi f q \Sigma \omega^2 r_p^4. \quad (25)$$

It is instructive to compare (25) with the corresponding expression for the prograde case,

$$T^p_{wave} \sim \frac{q^2}{\delta^2} \Sigma \omega^2 r_p^4. \quad (26)$$

From (25) we see that the ratio

$$T^r_{wave}/T^p_{wave} \sim \frac{\pi f \delta^2}{q}. \quad (27)$$

Thus, low mass objects immersed in the disk and rotating in different directions could drift with different radial velocities determined by the disk half-thickness and their mass ratios. In principal, this could lead to some interesting consequences, as e.g. a possibility of collision between the objects since, in this situation, for comparable mass ratios, the radial separation between them will in general decrease relatively rapidly with time.

5. Numerical simulations of embedded perturbers

We have performed numerical simulations using the 2D code NIRVANA (see e.g. Podlewska-Gaca et. al. 2012 and references therein) and also the ROe solver for Disk Embedded Objects (RODEO) method (see e.g. Paardekooper & Papaloizou 2009). In the context of results presented here, these independent methods were found to give almost identical results.

In this section we consider numerical simulations for which the perturber remained embedded without forming a significant gap. The initial surface density was specified to be $\propto r^{-1/2}$ and scaled so that the total mass interior to the initial orbital radius of the perturber was 10^{-3} in units of the dominant central mass. The perturber was initiated on a retrograde circular orbit of radius r_0 which is taken to be the simulation unit of length. For simulation unit of time we take the orbital period of a circular orbit with this radius. We adopted $H/r = 0.05$ and the kinematic viscosity was taken to be $\nu = 10^{-5} r_0^2 \Omega(r_0)$. The computational domain was taken to be $(0.2r_0, 5r_0)$. The outer radial boundary was taken to be rigid and the inner radial boundary open. Gravitational softening lengths ranging from $\Delta_s = 0.6H$, denoted as standard softening, to $\Delta_s = 0.1H$, denoted as small softening were considered. Grid resolutions with $N_R = 350$ and $N_\phi = 400$ equally spaced grid points in respectively the radial and azimuthal directions were typically adopted for cases with standard softening. For smaller softening lengths the resolution was increased to $N_R = 700$ and $N_\phi = 1200$. For simulations presented in this section, there was no accretion onto the perturber.

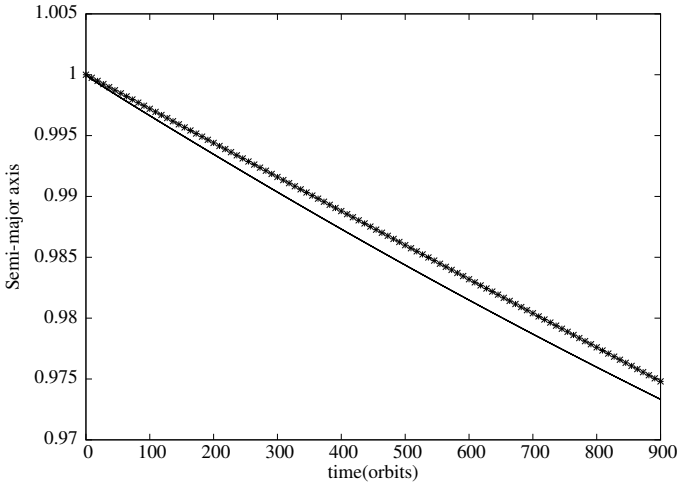

Fig. 1. Semi-major axis, in units of the initial orbital radius as a function of time orbits for $q = 0.001$. The solid curve give the results from numerical simulation and the curve with imposed crosses is obtained using equation(7) with contributions to the total torque for $m \leq 100$ obtained from equation (22). However, the main contribution comes from $m = 1$ in this case (see Section 5.1 below). The numerical simulation was performed with no accretion onto the companion.

The results of a numerical simulation that was performed for $q = 0.001$ for standard softening and with no accretion onto the perturber are illustrated in Fig.1. The semi-major axis, in units of the initial orbital radius is plotted as a function of time. In addition the evolution expected from the analytic theory, obtained from equation (7) with $|T|$ evaluated by summing the values of T_{wave} calculated using (22) for $m \leq 100$.

There is seen to be very good agreement between the two with the total amount of radial migration differing by less than 10% over 900 orbits. The form of the surface density after 100 and 840 orbits is illustrated in Fig.2. Apart from the central regions where the surface density becomes small on account of the outflow boundary condition, the surface density remains relatively unperturbed with low amplitude density waves being apparent in the vicinity of the orbit.

5.1. The dependence on the mass ratio and softening length

A comparison of orbital evolution rates calculated analytically as indicated above with those obtained from our numerical simulations for different mass ratios with standard softening and no accretion are presented in Table 1. In addition Fig. 3 indicates the contributions from $m = 1$ and all $m < 100$ to the analytic evolution rates. There is good agreement between the numerical and analytic results given in Table 1 which differ by not more than 25%, with the maximum deviation occurring for the smallest mass ratio case.

The dependence on the softening length was also investigated for the case with $q = 0.005$, and the results of a comparison between numerical and analytic migration rates are shown in Fig. 3. One can see that in this case there is a very good agreement between the analytical and numerical results down to softening lengths $\sim 0.1H$.

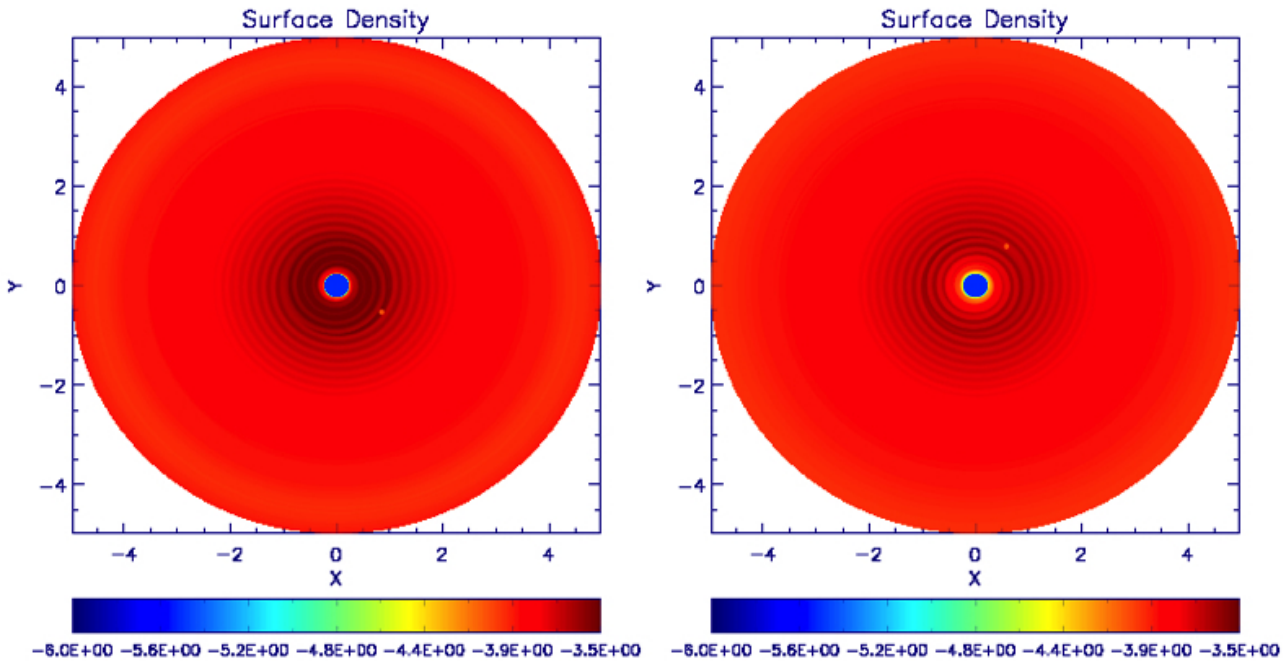

Fig. 2. $\log\Sigma$ contours for $q = 0.001$ with softening length $0.6H$ after 100 orbits (left panel) and after 840 orbits (right panel). In these simulations the companion, its position in each case being at the centre of the small superposed red circle, located on the line at an angle of $\sim 315°$ to the x axis (left panel) and at an angle of $\sim 45°$ to the x axis (right panel) was not allowed to accrete. Short wavelength density waves are visible on both sides of the quasi-circular orbit. The relative density changes are similar in both these plots. However, the density in the interior regions of the disk decreases at later times on account of accretion through the inner boundary.

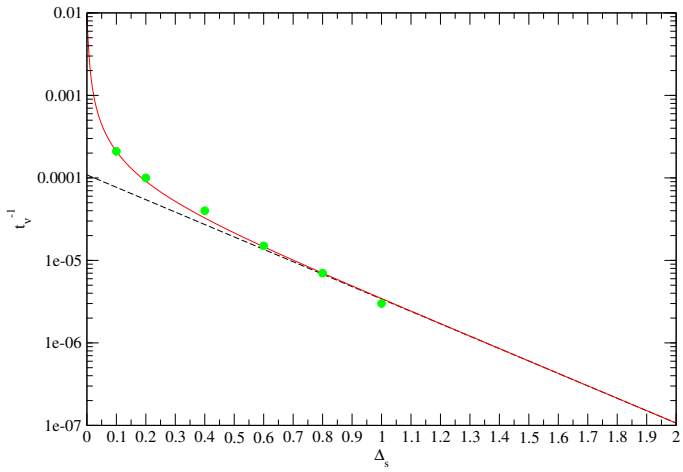

Fig. 3. The inverse of the evolution time scale defined according to equation (23), as a function of the dimensionless softening length Δ_s/H. It is expressed in units of P_0^{-1}, where P_0 is the initial orbital period of the perturber. The dashed line is calculated adopting equation (22) with only the contribution with $m = 1$ included. The solid line is calculated including contributions from all $m \leq 100$. The circles indicate the results of numerical simulations.

q	$(dr_p/dt)_n$	$(dr_p/dt)_a$
0.0001	-2.1e-6	-2.8e-6
0.0005	-1.6e-5	-1.4e-5
0.001	-3.4e-5	-2.8e-5
0.003	-7.9e-5	-8.3e-5

Table 1. The Table shows the evolution rates calculated numerically, $(dr_p/dt)_n$, and analytically as indicated above, $(dr_p/dt)_a$, for different values of the mass ratio q. The evolution rates, time averaged over several orbits and evaluated at early times, are in units $r_0 P_0^{-1}$, where P_0 is the initial orbital period of the perturber. The softening length for these calculations was taken to be $0.6H$.

6. Gap formation and migration for higher mass perturbers

We now consider perturbers massive enough to make the interaction between the disk and perturber non linear. We first consider simplified semi-analytic models for calculating gap profiles and migration rates, subsequently comparing results with direct numerical simulations.

6.1. A simplified description of the interaction between the perturber and disk

In general $\dot{J}$ can be determined by considering the disk response to the perturber as disk gas streams by. When dissipation is efficient enough to prevent angular momentum being carried away by waves, the process can be modelled as a direct transfer of angular momentum to the gas particles when they are scattered by the perturber while undergoing a close approach to it (see Lin & Papaloizou 1979). When dissipation is ineffective, the transferred angular momentum is carried away by waves which may dissipate in some other location making the process non local (see e.g. Papaloizou & Lin 1984). When the disk viscosity is small,

waves are expected to be excited when the perturbation is linear. On the other hand when the perturbation is non linear, shocks are likely to occur resulting in the local transfer of angular momentum.

For the regions of the disk where dissipation is effective locally, we adopt the impulse approximation employed by Lin & Papaloizou (1979) (see also Papaloizou & Terquem 2006) in the prograde case. However, here we modify the analysis to allow for the fact that the perturber moves in the direction opposite to that of the gas. Then we find that approximately

$$\dot{J} = -\frac{1}{4\pi}q^2(\Omega r)^2\frac{r^2}{\Delta^2+\Delta_s^2} \quad \text{when} \quad |\Delta| < r_c \quad \text{and}$$
$$\dot{J} = 0 \quad \text{when} \quad |\Delta| > r_c. \tag{28}$$

Here $\Delta = r - r_p$, and we have introduced a gravitational softening length, Δ_s, which prevents a divergence when $\Delta \to 0$.

The cut off radius r_c gives the distance inside which the perturbation is non linear and the impulse approximation can be employed. At greater distances we assume that the angular momentum transferred is carried away by waves and so does not affect the disk locally. We estimate that $r_c = min(r_h, r_s)$, where $r_h \approx (q/3)^{1/3}r_p$ is the Hill radius. The 'sound' radius, r_s, is defined through $r_s = (q/\delta)r_p$, where $\delta = H/r$ with H being the disk semi-thickness. This radius is defined as the impact parameter such that the radial velocity component of a gas particle induced by the scattering event is equal to the sound speed. When the sound radius exceeds the Hill radius, the latter is taken to be the cut off distance.

Note that the angular momentum carried away by waves does not affect the disk locally but should be taken into account when considering the evolution of the orbit. However, this is only a small effect once the interaction becomes significantly non linear as linearity then only applies at large scattering impact parameters for which the interaction is weak. Thus in that regime it may be neglected.

We here remark that the linear estimate (24) can be obtained from the above arguments based on treating the disk response to the perturber using the impulse approximation. To obtain it equations (5) and (28) are used under the assumption that the latter is approximately valid even when $\Delta \sim r_a$. Approximating (5), taking into account the disk on both sides of the perturber, as

$$T = 4\pi\Sigma r_p\int_{r_{min}}^{\infty}\dot{J}d\Delta \tag{29}$$

and making use of (28) with $\Delta_s = 0$, we recover the expression (24) when the inner cut off radius, $r_{min} \ll r_c$ is set equal to $2r_a/\pi$.

6.2. Evolution of the disk surface density

Multiplying equation (1) by $r^2\Omega$ and subtracting the result from (3) we obtain an expression for v_r in the form

$$v_r = \frac{2\dot{J}}{\Omega r} - \frac{3}{\Omega r^2\Sigma}\frac{\partial}{\partial r}(\nu\Omega r^2\Sigma), \tag{30}$$

and, accordingly,

$$\dot{L} = 2\pi r^2\left(3\Omega r\frac{\partial}{\partial r}(\nu\Sigma) - 2\Sigma\dot{J}\right), \quad \text{and}$$
$$\dot{M} = \frac{2\pi}{\Omega}\left(\frac{3}{r}\frac{\partial}{\partial r}(\nu\Omega r^2\Sigma) - 2\Sigma\dot{J}\right). \tag{31}$$

Substituting equation (30) into equation (1) and making use of (28) we obtain a single equation for the evolution of the surface density in the form

$$\frac{\partial\Sigma}{\partial t} = \frac{1}{r}\frac{\partial}{\partial r}\left(\frac{3}{\Omega r}\frac{\partial}{\partial r}(\nu\Omega r^2\Sigma) + \frac{q^2\Theta(D)\Sigma\Omega r^4}{2\pi(\Delta^2+\Delta_s^2)}\right), \tag{32}$$

where $\Theta(D)$ is the step function and $D = r_c - |\Delta|$.

It is convenient to introduce dimensionless variables $\tilde{r} = r/r_0$ and $\tilde{\Sigma} = \Sigma/\Sigma_0$, where r_0 and Σ_0 are the initial orbital radius of the perturber and surface density at its initial location, respectively. In addition we use $h = \sqrt{\tilde{r}}$ as spatial coordinate. We also assume power law dependences of ν on r and Σ through the relation

$$\nu = \nu_*\Sigma^a r^b = \nu_0\tilde{\Sigma}^a\tilde{r}^b = \nu_0\tilde{\Sigma}^a h^{2b}, \tag{33}$$

where ν_*, ν_0, a and b are constants. Then equation (32) takes the form

$$\frac{\partial\tilde{\Sigma}}{\partial\tau} = \frac{1}{h^3}\frac{\partial F}{\partial h}, \quad \text{with}$$
$$F = \frac{\partial}{\partial h}(h^{1+2b}\tilde{\Sigma}^{1+a}) + \beta\Theta(D)\frac{h^5\tilde{\Sigma}}{\tilde{\Delta}^2+\tilde{\Delta}_s^2}, \tag{34}$$

and

$$\tau = t/t_\nu, \quad \text{with} \quad t_\nu = \frac{4r_0^2}{3\nu_0}. \tag{35}$$

Here t_ν is a characteristic time scale of viscous evolution of the disk at $r \sim r_0$, $\beta = q^2\Omega_0 r_0^2/(3\pi\nu_0)$, $\Omega_0 = \Omega(r_0)$, $\tilde{\Delta} = \Delta/r_0$ and $\tilde{b} = b/r_0$.

From equations (31) and (34) it then follows that the mass and angular momentum fluxes can be expressed in the form

$$\dot{M} = \dot{M}_* F, \quad \dot{L} = \dot{L}_* h(F - h^{2b}\tilde{\Sigma}^{1+a}), \tag{36}$$

where $\dot{M}_* = 3\pi\Sigma_0\nu_0$ and $\dot{L}_* = \dot{M}_*\Omega_0 r_0^2$.

For our estimates below we use the standard representation of ν_0 through the Shakura-Sunyaev parameter α (Shakura (1973), Shakura & Sunyaev (1973))as

$$\nu_0 = \alpha\delta^2\Omega_0 r_0^2. \tag{37}$$

The coefficient ν_* defined through (33) can then be expressed in terms of quantities characterising opacity law in the disk and α, for an explicit expression see Lyubarskiy & Shakura (1987) and IPP. From equation (37) we obtain

$$t_\nu \approx \alpha^{-1}\delta^{-2}\Omega_0^{-1} \quad \beta \approx 0.1\frac{q^2}{\alpha\delta^2} \tag{38}$$

6.3. Initial and boundary conditions for a disk structured by a perturber

We assume that the disk is in a steady state at time $t = 0$ when the binary is introduced. In the steady state the dependence of $\tilde{\Sigma}$ on h follows from equations (34) with time derivatives and q set to zero. Thus $dF/dh = 0$, and therefore

$$\Sigma = \Sigma_0 h^{-\frac{1+2b}{1+a}} (F_0(h-1)+1)^{\frac{1}{1+a}}, \tag{39}$$

and

$$\dot{M} = \dot{M}_* F_0, \quad \dot{L} = \dot{L}_*(F_0 - 1), \tag{40}$$

where F_0 is a constant of integration and we have ensured that $\Sigma(h=1) = \Sigma_0$ as required by definition. Of special interest are the cases with $F_0 = 1$ and $F_0 = 0$. These correspond to cases with zero angular momentum flux and zero mass flux through the disk, respectively. The former case corresponds to a disk of formally infinite extent with constant mass flux equal to $\dot{M}_*$. Recalling that the angular momentum flux in a stationary disk is determined by an inner boundary condition and is typically small, we can consider the case $F_0 = 0$ as appropriate for astrophysical systems of interest such as a disk interacting with a binary black hole since we expect the secondary to be immersed in the disk at radii much larger than its inner boundary radius [2].

The case with $F_0 = 0$ can approximately describe a circumbinary disk around a massive binary rotating in the same sense as the disk gas (e.g. Ivanov, Papaloizou & Polnarev 1999). Although there is no direct relation to situations considered in this Paper, we use $\tilde{\Sigma}$ distributions for such models in several numerical runs to test different initial conditions.

It is instructive to express the steady state surface density and the angular momentum flux in terms of the mass flux, the quantity $h_* = (F_0 - 1)/F_0$ and the viscosity coefficient ν_* defined through (33). We obtain

$$\Sigma = \left(\frac{\dot{M}}{3\pi\nu_* r_0^b}\right)^{1/(1+a)} h^{-(1+2b)/(1+a)} (h-h_*)^{1/(1+a)} \text{ with}$$
$$\dot{L} = \dot{M}\Omega_0 r_0^2 h_*. \tag{41}$$

From (41) it is clear that $h = h_*$ corresponds to the inner edge of the disk, where the surface density drops to zero.

Because we cannot perform two dimensional numerical simulations of accretion disks of arbitrary radial extent, we develop an approximate theory of the evolution of the disk and orbit that is valid both for disks of finite and infinite extent. This will be tested against numerical simulations for the case of disks of finite extent.

6.4. Conditions for gap formation

The action of the impulsive torque per unit mass exerted on the disk by the perturber given by (28) is to cause gas elements to lose angular momentum as they encounter and are scattered by the perturber. This causes them to move to smaller radii, enhancing any inward drift resulting from viscous evolution. Since the disk gas in the vicinity of the orbit is supplied from the outer regions of the disk at a rate determined by viscous evolution and the presence of the perturber increases the magnitude of the radial velocity, v_r, that is directed inwards, a surface density depression must form close to the perturber orbit in order that the continuity equation be satisfied. We hereafter describe this depression as 'a gap' but emphasise that the way the gap is formed differs from that applicable to the well known case when the perturber is in a prograde orbit (see eg. Papaloizou & Terquem 2006).

As indicated above, the impulsive torque is efficient only when the distance from the perturber, Δ is smaller than both the Hill radius $r_h \approx (q/3)^{1/3} r_p$ and 'the sound radius', $r_s \sim (q/\delta) r_p$. When the mass ratio is very small, and, accordingly, impulsive interactions are not effective, the angular momentum transferred between the perturber and disk is transported away by waves and a pronounced gap in the disk is not produced.

We make a simple estimate for when this should occur by requiring that r_s should be smaller than $\pi\delta r_p/2$, which is half the longest wavelength associated with density waves launched by the perturber which occurs for $m = 1$ (see above). This gives $r_s < \pi\delta r_p/2$ from which we obtain

$$q < q_1, \quad q_1 = \frac{\pi}{2}\delta^2 \approx 1.57\delta^2. \tag{42}$$

We emphasise that on account of it being obtained from simple estimates, this criterion is uncertain to within a numerical factor of order unity. Nonetheless we found that our numerical results are in agreement with it. We adopted $\delta = 0.05$ in our numerical calculations. Then we obtain $q_1 \approx 5 \cdot 10^{-3}$. We observed gap formation in the case of the somewhat larger $q = 0.01$ and did not observe it for $q = 0.001$.

6.4.1. Secondary mass larger than the local disk mass

In the opposite limiting case of a large mass ratio such that the secondary mass M_p is much larger than a characteristic disk mass within its orbital radius $M_d \equiv \dot{M}_* t_\nu = 4\pi\Sigma_0 r_0^2$, the local viscous evolution time scale of the disk is expected to be much smaller than the evolution time scale of the binary orbit. In this case one may find the time scale for evolution of the orbit in two steps. At first, one can determine the modification of the disk structure induced by the binary assuming that its separation distance r_p is fixed and then calculate the interaction torque T. One can use this in equation (7) to find the evolution time scale. From the condition $M_p > M_d$ we obtain

$$q > q_2, \quad q_2 = \frac{4\pi\Sigma_0 r_0^2}{M}. \tag{43}$$

6.4.2. Issue of gravitational stability

Note that the ratio of the local disk mass, M_d, to the mass of the primary should be of the order of or smaller than δ for the disk to be gravitationally stable according to the Toomre stability criterion. It is, therefore, sufficient to have

$$q > q_{crit} = \delta \tag{44}$$

for q to be larger than both q_1 and q_2. Note that this case is analogous to what is considered in Ivanov et al. (1999)

[2] For example, for a black hole and a 'standard' accretion disk we have $\dot{L} = \dot{M}\sqrt{GMr_{ms}}$, where r_{ms} is the radius of the marginally stable orbit. Clearly, it is much smaller than $\dot{L}_*$ when $r_0 \gg r_{ms}$.

for systems with prograde rotation. For supermassive black hole masses appropriate to galactic centres inequality (44) typically holds.

7. Simple 1D modelling of the surface density profile for the case of relatively large mass ratio

In this Section we assume that although the mass ratio $q \ll 1$ the conditions $q > q_1$ and (43) are both fulfilled, and, accordingly, the ratio of the perturber mass to a characteristic mass of the disk is large. As we discussed above, in this situation the characteristic time for evolution of the perturber's orbit is much larger than that of the disk, so that in order to model the evolution in a simple way, we can calculate quantities characterising the evolution of the system iteratively, assuming at first that the perturber's orbital distance is fixed and analysing properties of the disk, and then calculating the evolution rate of the binary.

7.1. Structure of the gap around perturber's orbit obtained by solving the diffusion equation incorporating the effect of torques due to the perturber

As we have seen, a depression in the profile of the surface density called a gap is formed in the neighbourhood of the perturber's orbit. Gravitational interaction with the perturber removes angular momentum from disk gas elements as they stream past it, thus increasing their radial drift velocity in the vicinity of the orbit. The formation of the gap can be described by equation (34) which incorporates the effects of viscosity and torques due to the perturber. It may be shown that after some relatively short period of time the solution to (34) in the neighbourhood of $r \sim r_p$ becomes quasi-stationary. This implies that in order to find the form of $\tilde{\Sigma}$, we can assume that the dimensionless mass flux, F, defined there, does not depend on the radial coordinate h, and, accordingly, obtain an equation for $\tilde{\Sigma}$ of the form

$$\frac{d}{dx}\left(\tilde{\Sigma}^{1+a}\right) + \beta \frac{\tilde{\Sigma}}{4x^2 + \tilde{\Delta}_s^2} = F, \qquad (45)$$

where $x = h - 1$, the ratio r_c/r_0 is assumed to be small and we also consider the region, where $\tilde{\Delta} \leq r_c/r_0$, and, accordingly, the coordinate x should be such that $x_- \leq x \leq x_+$, where $x_\pm = \pm r_c/(2r_0)$.

Note that the condition (44) together with equation (38) imply that for $\alpha < 0.1$, β should be of the order of or larger than unity, and in the limit that $q \gg q_{crit}$ we accordingly have $\beta \gg 1$.

Since a detailed shape of $\tilde{\Sigma}$ close to the orbit does not influence our results, we consider in this Paper, for simplicity, only the linear case $a = 0$, for which the general solution to (45) can be written down in the form

$$\tilde{\Sigma} = \exp(-\beta \tan^{-1} y/(2\tilde{\Delta}_s)) \left(C + \frac{\tilde{\Delta}_s F}{2} \times \right.$$
$$\left. \int_0^y dy' \exp(-\beta \tan^{-1} y'/(2\tilde{\Delta}_s)) \right), \qquad (46)$$

where $y = 2x/\tilde{\Delta}_s$ and C is an integration constant.

In general the integral in (46) can be expressed in terms of hypergeometric functions, but the resulting expression is cumbersome and difficult to use. The expression simplifies, however, when $\tilde{\Delta}_s = 0$. In this case we have

$$\tilde{\Sigma} = \frac{\beta F}{4}\left(\frac{1}{z} - e^z \mathrm{E}_1(z)\right) + C_+ e^z \quad \text{for} \quad x > 0,$$
$$\tilde{\Sigma} = \frac{\beta F}{4}\left(e^{-z}\mathrm{Ei}(z) - \frac{1}{z}\right) + C_- e^{-z} \quad \text{for} \quad x < 0, \qquad (47)$$

where $z = \beta/(4|x|)$,

$$\mathrm{E}_1(z) = \int_z^\infty \frac{e^{-t}}{t} dt \quad \text{and}$$
$$\mathrm{Ei}(z) = \int_{-\infty}^z \frac{e^t}{t} dt \qquad (48)$$

When $x \to 0$, $z \to \infty$ the term proportional C_+ diverges exponentially. That means that we have to set $C_+ = 0$. In this case we have $\tilde{\Sigma}(x = 0) = 0$.

When $\tilde{\Delta}_s \neq 0$ the expression for $\tilde{\Sigma}$ is different from (47) with the most important qualitative difference due to the fact that in this case the value of the surface density at its minimum is non-zero. Assuming that the position of the minimum, $x = x_m < \tilde{\Delta}_s$, from equation (45) it follows that $\tilde{\Sigma}(x_m) \approx \tilde{\Delta}_s^2 F/\beta$. On the other hand $\tilde{\Sigma}(x_m)$ is much smaller than other terms in the expression (47) when $x/\tilde{\Delta}_s \gg 1$, and, therefore, to account approximately for a non-zero value of the minimum we simply add $\tilde{\Sigma}(x_m)$ to the expression given by (47). In this way we finally obtain

$$\tilde{\Sigma} \approx \frac{\beta F}{4}\left(\frac{1}{z} - e^z \mathrm{E}_1(z) + 4\frac{\tilde{\Delta}_s^2}{\beta^2}\right) \quad \text{for} \quad x > 0,$$
$$\tilde{\Sigma} = \frac{\beta F}{4}\left(e^{-z}\mathrm{Ei}(z) - \frac{1}{z} + 4\frac{\tilde{\Delta}_s^2}{\beta^2}\right) + C_- e^{-z} \text{ for } x < 0. \qquad (49)$$

The value of the variable z, corresponding to the boundary values of x of the zone where the impulsive interactions operate, $x_\pm = \pm r_c/(2r_0)$, namely $z_b = \beta r_0/(2r_c)$, is expected to be large. Since $z \geq z_b$ throughout the region $x_- \leq x \leq x_+$ when $z_b \gg 1$, we can simplify the expression (49) using the corresponding asymptotic expressions of the functions $\mathrm{E}_1(z)$ and $\mathrm{Ei}(z)$ for large z. In this way we get

$$\tilde{\Sigma} \approx \frac{F}{\beta}(4x^2 + \tilde{\Delta}_s^2) \quad \text{for} \quad x > 0,$$
$$\tilde{\Sigma} = \frac{F}{\beta}(4x^2 + \tilde{\Delta}_s^2) + C_- e^{-z} \quad \text{for} \quad x < 0, \qquad (50)$$

and we recall that $\tilde{\Delta} = (r - r_0)/r_0 = 2x$.

From (50) it follows that when F is fixed, $\beta \to \infty$ and $\Delta_s \to 0$, all terms in (50) tend to zero apart from the term, proportional to the constant C_-, which can be made arbitrary large. This means that when q is large we expect the surface density at the outer edge of the gap to be small compared to the surface density at the inner edge where there is a jump in $\tilde{\Sigma}$ of magnitude C_-.

However, as we shall see below, the above analysis predicts a minimum surface density in the gap that is too low. We investigate the possibility that this is because the scattering process is not entirely localised at one radial location as has been assumed. This effect is expected to have greater significance close to the perturber.

7.1.1. Modification of the gap profile close to the perturber

When the dimensionless distance from the perturber, $\tilde{\Delta}$, is sufficiently small, equation (34) may not be adequate for describing the surface density distribution. We remark that from equation (28) it follows that during one orbital period the quantity, $\tilde{\Delta}$, for a particular gas element changes according to

$$\delta\tilde{\Delta} = \frac{2P_{orb}\dot{J}}{\sqrt{GMr_0}} = -\frac{q^2}{\tilde{\Delta}^2 + \tilde{\Delta}_s^2}. \quad (51)$$

When $\tilde{\Delta}$ is sufficiently small, the magnitude of $\delta\tilde{\Delta}$ can be of the order of the magnitude of $\tilde{\Delta}$ itself. In this situation a particular gas element crosses the perturber position such that $\tilde{\Delta} < 0$. Then every relative period the surface density associated with this element changes by order of itself until $|\tilde{\Delta}|$ becomes large enough so that $|\delta\tilde{\Delta}|$ becomes small compared to $|\tilde{\Delta}|$.

Clearly, we expect a non-zero value of the surface density even when $\tilde{\Delta}_s = 0$ and equation (50) predicts that $\tilde{\Sigma}(\tilde{\Delta} = 0) = 0$. From the condition $|\tilde{\Delta}| < |\delta\tilde{\Delta}|$ we have

$$\tilde{\Delta} < \tilde{\Delta}_* = q^{2/3}, \quad (52)$$

and the value of the surface density at $\tilde{\Delta} = 0$ may be simply estimated with the help of equation (50) as

$$\tilde{\Sigma}_{min} \equiv \tilde{\Sigma}(\tilde{\Delta} = 0) \sim \tilde{\Sigma}(\tilde{\Delta}_*) \sim q^{4/3}\frac{F}{\beta}. \quad (53)$$

We comment that we have here simply assumed that the azimuthally averaged Σ does not decrease below the value at $\tilde{\Delta} = \tilde{\Delta}_*$. This ignores azimuthally localised phenomena such as accretion onto the perturber but this is not found to affect the azimuthally averaged profile much in 2D simulations.

Let us consider this effect in more detail. We first introduce a new variable $y = q^{-2/3}\tilde{\Delta}$ and consider a map defined by

$$y_{n+1} = y_n - \frac{1}{y_n^2 + y_s^2}, \quad (54)$$

where $y_s = q^{-2/3}\tilde{\Delta}_s$. Here y_n denotes the value of y obtained after n iterations, the starting value being y_0. This map describes successive changes to y for a gas element occurring as a result of scattering, obtained by application of (51). The corresponding values of the surface density $\tilde{\Sigma}_{n+1}$ and $\tilde{\Sigma}_n$ are related through conservation of mass such that $\tilde{\Sigma}_{n+1}dy_{n+1} = \tilde{\Sigma}_n dy_n$:

$$\tilde{\Sigma}_{n+1} = \frac{\tilde{\Sigma}_n}{(1 + 2y_n/(y_n^2 + y_s^2)^2)}. \quad (55)$$

The map (54) and (55) can be iterated from some initial $y_0 \gg 1$, where the distribution (50) is valid, and we have, accordingly,

$$\Sigma = \Sigma_*(y_0^2 + y_s^2), \quad \Sigma_* = q^{4/3}\frac{F\Sigma_0}{\beta}. \quad (56)$$

We iterate the map numerically starting from several initial values of y_0 to take into account a dependence of this procedure on initial conditions. They are chosen according to the rule: $y_0 = 20 + dy(i-1)$, $dy = 0.01528\pi$ and $i = 1, 2, 3..N$. An iteration proceeds until $y_n < 0$. Then, we define a minimum surface density corresponding to a particular y_0 as $\Sigma^i_{min} = 0.5(\Sigma_n + \Sigma_{n-1})$. We then further average over the results obtained for different y_0. The result of this calculation is shown in Fig. 4, where we plot the quantity

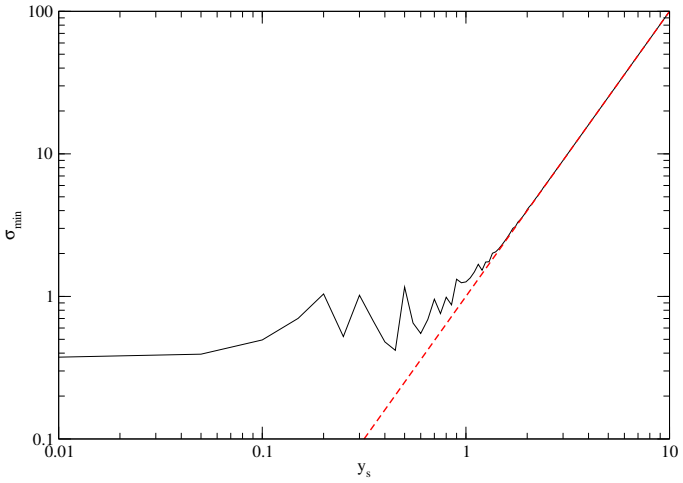

Fig. 4. The dependence of the mean ratio of the minimum surface density in the gap, to the characteristic disk surface density Σ_*, σ_{min}, as a function of the parameter y_s. The solid curve represents the result obtained from the numerical iterations of the map based on the solution of equations (54) and (55), while the dashed curve shows the analytic expression $\sigma_{min} = y_s^2$.

$$\sigma_{min} = \frac{1}{N\Sigma_*}\sum_{i=1}^{N}\Sigma^i_{min}. \quad (57)$$

for $N = 1000$.

As seen from Fig. 4 we can approximate the dependence of σ_{min} on y_s as [3]

$$\sigma_{min}(y_s < 1) \approx 0.4, \quad \sigma_{min}(y_s > 1) \approx y_s^2. \quad (58)$$

From equations (56) and (58), together with the definition of the parameter β, we can obtain an estimate of the minimum surface density in the gap as

$$\Sigma_{min}(y_s < 1) \approx \frac{1.2\pi q^{-2/3}F\nu_0\Sigma_0}{\Omega_0 r_0^2},$$
$$\Sigma_{min}(y_s > 1) \approx \frac{3\pi F\nu_0\Sigma_0}{\Omega_0 r_0^2}\left(\frac{\tilde{\Delta}_s}{q}\right)^2. \quad (59)$$

We emphasise the approximate nature of these estimates which are found to be in general too small by a factor of a few (see below). This is probably on account of the neglect of smoothing of the profile due to the action of pressure. Finally we would like to stress that although we effectively assumed above that the orbital radius of perturber r_p is close to its initial value r_0, the analytic expressions are valid for any r_p, by simply replacing r_0 by r_p in them.

[3] Clearly, there is some transitional zone in the region $0.1 < y_s < 2$, where σ_{min} varies in a complicated way. Since we need only a crude estimate of σ_{min} we neglect this feature.

8. A simple procedure for calculating the accretion disk evolution together with the orbital evolution of the perturber occurring through torques exerted by the disk

As discussed above, after the perturber has been present in the disk for a time that is larger than its characteristic evolution time scale, but smaller than the characteristic time scale for orbital evolution, the disk structure at radii, $r \sim r_p$, should be close to a quasi-stationary one. In this situation, the mass flux $\dot{M}$ and the dimensionless value of the specific angular momentum at the inner disk that appears in equation (41) may be assumed to be functions of time only with a characteristic time scale for change being much larger than that required for local disk evolution.

On the other hand, in the limit $q \ll 1$ the region in the vicinity of perturber, where impulsive interaction operates, is very small, with a typical dimension $\ll r_p$. Therefore, in the simplest treatment of the problem we describe the influence of the perturber on the disk as providing a jump condition on the surface density, to be applied at the perturber's orbital location, in a disk otherwise evolving only under the influence of internal viscosity.

As indicated above, the mass flux through the gap is approximately constant in this limit. In addition, from the steady state solution given by equation (41) it can be seen that when the mass flux is fixed, stationary solutions depend only on one constant, h_*, which is proportional to the flux of angular momentum through the disk $\dot{L} = \dot{M}\Omega_0 r_0^2 h_*$.

In Section 7 we showed that the outer disk for which $r > r_p$ should attain $\Sigma(r_{p+}) \sim 0$ (see discussion in the penultimate paragraph of section 7.1). This means that the flux of angular momentum through the disk at radii $r > r_p$ and $r \sim r_p$, $\dot{L}_+$, should be $\sim \dot{M}\sqrt{GMr_p}$ and we must set $h_* = \sqrt{r_p/r_0}$ in equation (41) in order for this to be applicable to the outer disk.

On the other hand, the flux of angular momentum through the inner disk, at radii $< r_p$, $\dot{L}_-$, should be equal to the angular momentum accreted per unit time by the component with the dominant mass, M. Assuming that r_p is much larger than the size of the last stable orbit of that component, we can set $\dot{L}_- \approx 0$. Therefore, we set $h_* = 0$ in equation (41) in order to apply that to the inner disk located at radii $r < r_p$.

We accordingly obtain

$$\Sigma(r) = \left(\frac{\dot{M}(t)}{3\pi\nu_* r_0^b}\right)^{1/(1+a)} h^{-2b/(1+a)}, \quad \text{for} \quad r < r_p \quad \text{and}$$

$$\Sigma(r) = \left(\frac{\dot{M}(t)}{3\pi\nu_* r_0^b}\right)^{1/(1+a)} h^{-(1+2b)/(1+a)} \left(h - \sqrt{r_p/r_0}\right)^{1/(1+a)}$$

$$\text{for} \quad r > r_p. \tag{60}$$

We remark that the first of these solutions appropriate to the outer disk corresponds to a steady state disk with zero couple at $r = r_{p+}$, while the second solution appropriate to the inner disk corresponds to a steady state disk with zero couple at a very small inner boundary radius.

For $r < r_p$, equation (60) gives the value of the surface density at the inner edge of the gap for the linear case with $a = b = 0$ as

$$\Sigma(x = x_-) \approx \frac{\dot{M}(t)}{3\pi\nu_*}. \tag{61}$$

This can be used to obtain an estimate the constant C_- entering (47). In particular, in the limit $\beta \to \infty$, for finite F, C_- becomes equal to $\Sigma(x = x_-)$.

We stress again that the solution (60) is approximately valid only at scales such that r is of order r_p. It clearly becomes invalid at a length scale which is large enough that the characteristic time scale for evolution of the disk t_{diff} becomes equal to or larger than the time t after which either the perturber embedded in the disk, or changes its orbital radius by an amount comparable to r_p. To calculate the disk evolution at large radii it is necessary to use equation (34) with the time dependence retained.

Since the total angular momentum of the system is conserved and there is no angular momentum flux through the inner disk, the outward angular momentum flux through the outer disk, T, must be equal and opposite to the torque acting on the perturber due to the disk, the latter thus being $-T$. We have, therefore,

$$T \approx -\dot{M}(t)\sqrt{GMr_p} \tag{62}$$

and we recall that as $\dot{M}(t) > 0$, $T < 0$ (see section 3.2).

8.1. Evolution of the surface density in the outer disk

In order to model the evolution of the disk surface density together with the orbital evolution of the binary, we implement a procedure that updates the disk surface density using equation (34) with the torque terms corresponding to interaction with the disk being set to zero.

In our analytical work we have so far assumed, for simplicity, that the binary semi-major axis, r_p, is close to its initial position, r_0. However, many expressions, such as e.g. the distribution of the surface density in the gap, remain approximately valid even when r_p is noticeably smaller than r_0, provided that we substitute r_p for r_0. This can be understood as follows. When the perturber is sufficiently heavy, from the discussion in the previous section, the solution close to its orbit is quasi-stationary, such that the fact that at any time r_p is changing, plays only a minor role. In this situation, it is convenient to change the unit of length in (34) from r_0 to r_p, neglecting $\dot{r}_p$ when carrying out this transformation. Accordingly, from now on we switch the unit of length from r_0 to r_p in the definition of the variable h in (34) so that $h = \sqrt{r/r_p}$. This coincides with the previous definition $h = \sqrt{r/r_0}$ only when $t = 0$. Other quantities are appropriately rescaled apart from those involving Σ_0, which as before denotes the initial surface density at $r = r_0$. Then we can continue to use the kinematic viscosity prescription defined through (33). We further remark that when these changes are made, the second term in brackets in the second expression in (60) is equal to unity.

Under the above conditions equation (34) gives the equation for the evolution of the surface density as

$$\frac{\partial\tilde{\Sigma}}{\partial\tau} = \frac{1}{h^3}\frac{\partial^2\Phi}{\partial h^2} \quad \text{with} \quad \Phi = h^{1+2b}\tilde{\Sigma}^{1+a}. \tag{63}$$

in the region $h > 1$ with the initial conditions defined by equation (39) and the inner boundary condition

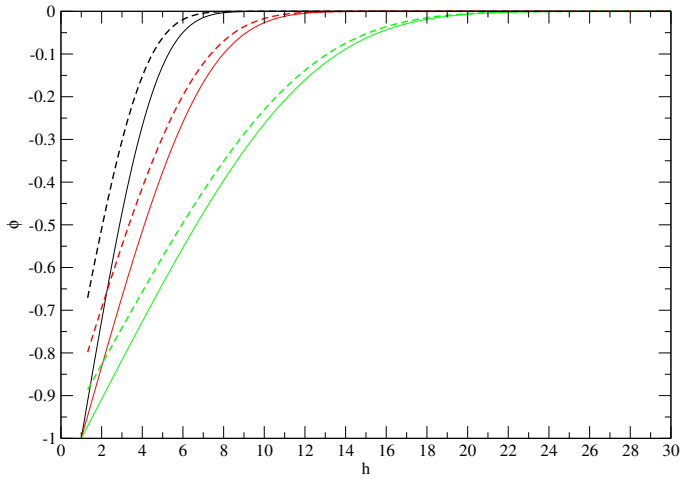

Fig. 5. The difference $\phi = \Phi - h$ is shown as a function of the radial coordinate h, at $\tau = 5$, 20 and 100, see the text for details.

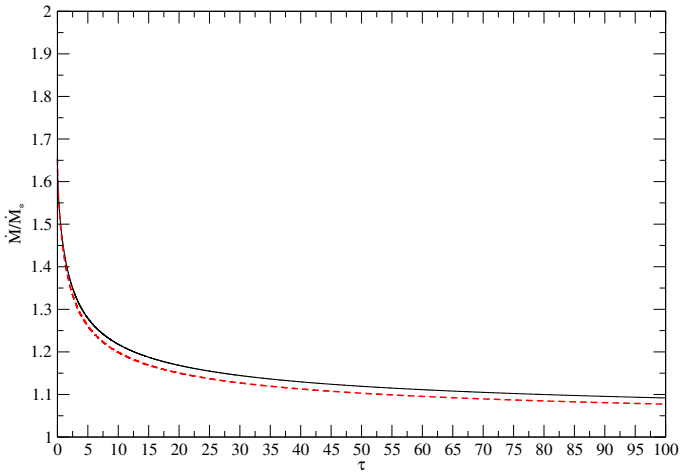

Fig. 6. The dimensionless mass flux $\dot{M}/\dot{M}_*$ is shown as a function of time τ. The solid and dashed curves correspond to $a = 2/3$, $b = 1$ and $a = 3/7$, $b = 15/14$, respectively.

$\tilde{\Sigma}(h = 1) = \Phi(h = 1) = 0$. [4]. We adopt an outer boundary condition that either corresponds to a disk of formally infinite extent or corresponds to a finite boundary at an outer radial distance, taken to be $h_{out} = \sqrt{5}$. In the former case we assume that asymptotically, when $h \to \infty$ the angular momentum flux tends to zero, i.e. the disk approaches the solution (39) with $F_0 = 1$. Then, we find the mass flux using equation (36) with $F = \partial\Phi/\partial h$. In the latter case we assume that there is no mass flux through the outer boundary at $h_{out} = \sqrt{5}$. The results obtained with this boundary condition can be directly compared with numerical simulations, most of which adopted this boundary condition.

While the surface density is being updated using the above procedure, we use equations (6), (7) and (62) to simultaneously find the orbital evolution of the perturber. However, note that after the unit of length has been changed from r_0 to r_p, the value of h_{out} corresponding to a fixed pre-scaled radius grows with time. The effect of this can be taken into account within the framework of our approximation scheme by use of a grid of solutions to (63) corresponding to different h_{out}. The situation can be further simplified for the case of a constant kinematic viscosity when equation (63) becomes linear. In this case, its late time solution is mainly determined by the smallest eigenvalue of the linear eigenvalue problem determining the associated normal modes. The dependence of this on h_{out} is discussed in the Appendix where it is illustrated in Fig. A.1. In our numerical work we have only considered modest changes of r_p for which this effect turns out to be unimportant. It is not, accordingly, taken into account in the rest of the Paper.

[4] Note that in fact the initial distribution (39) is not compatible with the inner boundary condition, accordingly, in practice, when solving (63) numerically we modify the stationary solution (39) by adjusting the surface density profile within a small transitional region $1 \le h \le 1 + \Delta h$, $\Delta h < 1$, in order that $\tilde{\Sigma}(h = 1) = 0$. An exact form of the surface density profile in the transitional region is not important for the solution at large time $\tau > 1$.

8.2. A similarity solution for an accretion disk of infinite extent

For arbitrary a and b, equation (63) has in general to be solved numerically. However, simple arguments allow us to show that when $\tau \gg 1$ the accretion rate close to the perturber is approximately equal to that at infinity. In order to find the corresponding approximate non-stationary solution to (63) we note that it must have the property that

$$\Phi(r) \sim h - 1, \quad \text{for } r < r_{diff}(\tau) \quad \text{and}$$
$$\Phi(r) \to h \quad \text{for } r \to \infty \tag{64}$$

to satisfy the inner boundary condition and the requirement that the disk tends asymptotically to the stationary solution with zero angular momentum flux. We recall that $r_{diff}(\tau)$ is the radius at which the local viscous diffusion time is equal to the current time τ in dimensionless form. Assuming that $r_{diff} \gg r_p$ the difference $\phi = \Phi - h$ should be small at $r > r_{diff}$ and we can treat it as a perturbation. In this case we can obtain a linear equation for ϕ by linearizing (63). This takes the form

$$\frac{\partial\phi}{\partial\tau} = (a+1)h^{\frac{2(b-(a+1))}{a+1}}\frac{\partial^2\phi}{\partial h^2}. \tag{65}$$

We look for a self-similar solution to (65) of the form $\phi = \phi(\xi)$, where the similarity variable $\xi = h\tau^{-\gamma}$ and $\gamma = (a+1)/2c$, with $c = 2(a+1) - b$. The function ϕ then satisfies the ordinary differential equation

$$\frac{d^2\phi}{d\xi^2} + \frac{1}{2c}\xi^{\frac{3(a+1)-2b}{a+1}}\frac{d\phi}{d\xi} = 0 \tag{66}$$

and we assume from now on that $c > 0$. Note that $r_{diff}(\tau)$ can be found from the requirement $\xi(r_{diff}, \tau) = 1$ and we, accordingly, have $r_{diff} = r_p\tau^{2\gamma}$. The general solution to (66) is

$$\phi = C_1 + C_2\int_0^\xi d\eta \exp\left(-(a+1)\eta^{\frac{2c}{a+1}}/(4c^2)\right). \tag{67}$$

where C_1 and C_2 are constants of integration. These are determined by the requirement that the solution should

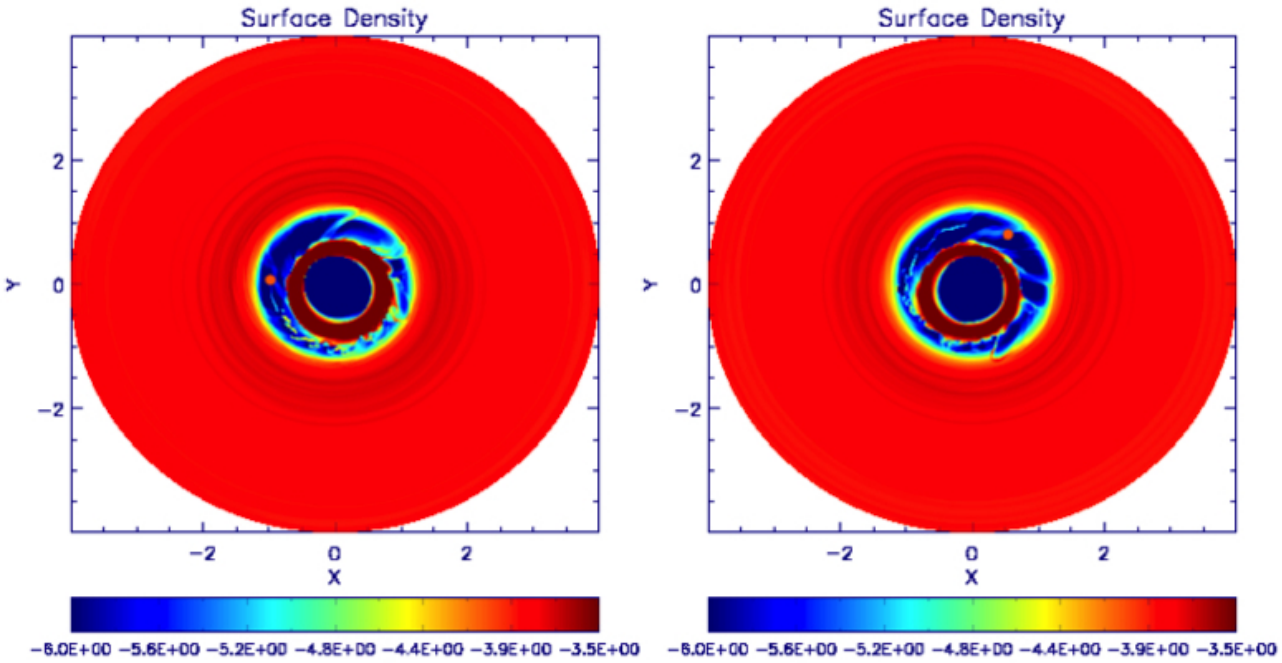

Fig. 7. $\log\Sigma$ contours for $q = 0.02$ with softening length $0.1H$ after 50 orbits (left panel) and after 100 orbits (right panel). In these simulations the companion, its position in each case being at the centre of the small red circle located within the gap region, was allowed to accrete. The width of the gaps slowly increase while the accretion rates, on average, slowly decrease with time. Short wavelength density waves in the outer disks are just visible. Note that values of $\log\Sigma$ below the minimum indicated on the colour bar are plotted as that minimum value

satisfy the conditions that $\phi \to -1$ for $\xi \to 0$ and $\phi \to 0$ for $\xi \to \infty$[5]. These ensure that the surface density profile matches the required forms for $h = 1$ as $\tau \to \infty$, and $h \to \infty$ for all τ. We therefore find

$$\phi = \frac{1}{I}\int_0^{\xi} d\eta \exp\left(-(a+1)\eta^{\frac{2c}{a+1}}/(4c^2)\right) - 1, \qquad (68)$$

where

$$I = \int_0^{\infty} d\eta \exp\left(-(a+1)\eta^{\frac{2c}{a+1}}/(4c^2)\right)$$
$$= \frac{(a+1)}{2c}\left(\frac{a+1}{4c^2}\right)^{-\frac{(a+1)}{2c}} \Gamma((a+1)/2c) \qquad (69)$$

with Γ denoting the gamma function.

In order to demonstrate the applicability of the similarity solution described above, we illustrate a numerical solution of equation (63) in Figs. 5 and 6. In Fig. 5 the quantity $\phi = \Phi - h$ is shown at times $\tau = 5$, 20, 100 with curves passing through larger values at the same h corresponding to later times. The solid curves are obtained by numerical solution of equation (63) while the dashed curves represent the analytical expression (68). For the solution shown, $a = 2/3$ and $b = 1$ which are the values expected for a disk with Thompson opacity being dominant. For initial condition we took $\Phi = h$, with the adjustment as described in section 8.1 , which corresponds to the distribution given by (39) with $F_0 = 1$.

One can see that the quantity ϕ does have the form predicted by the expression (68). It tends to -1 at small values of h and to zero at large values of h with intermediate values being gradually shifted towards larger h with time. In Fig. 6 the dimensionless mass flux $\dot{M}/\dot{M}_*$, where $\dot{M}_* = 3\pi\Sigma_0\nu_0$, is shown as a function of time for the case $a = 2/3$, $b = 1$ (solid curve) and the case of $a = 3/7$ and $b = 15/14$, the latter corresponding to a disk opacity dominated by free-free transitions. It is clear that the mass flux tends asymptotically to its unperturbed value when $\tau \to \infty$. It can be also seen that the ratio $\dot{M}/\dot{M}_*$ never exceeds ~ 1.6 for all times.

9. Orbital evolution time scale

Since the time dependent mass flux never significantly exceeds its unperturbed value, and tends asymptotically to this value, we estimate the mass flux in (62) as $\dot{M}(t) \approx \dot{M}$, where $\dot{M}$ is the unperturbed mass flux, i.e. the one that existed in the disk before the secondary had been embedded. Substituting the result for T in equations (6) and (7) we get

$$r_p = r_0 \exp\left(-t/t_{ev}\right), \quad t_{ev} = \frac{M_p}{2\dot{M}}. \qquad (70)$$

Thus, in this case the orbital evolution time scale is equal to the time that would be required for the steady state accretion flow through the unperturbed disk to amount to half of the perturber mass, $M_p/2$. We comment that this evolution time scale was given by Nixon et al. (2011) and Roedig et al. (2014) (see equation (9) in the latter paper in the limit of small mass ratio and small eccentricity with no accretion onto the perturber). This was obtained by simply assuming that mass flowing through the orbit transfers *all* its angular momentum to the companion. Here we have considered the

[5] Note that the inner boundary condition formally assumes that $r_p \approx 0$ and is approximately valid only when $r_{diff} \gg r_p$.

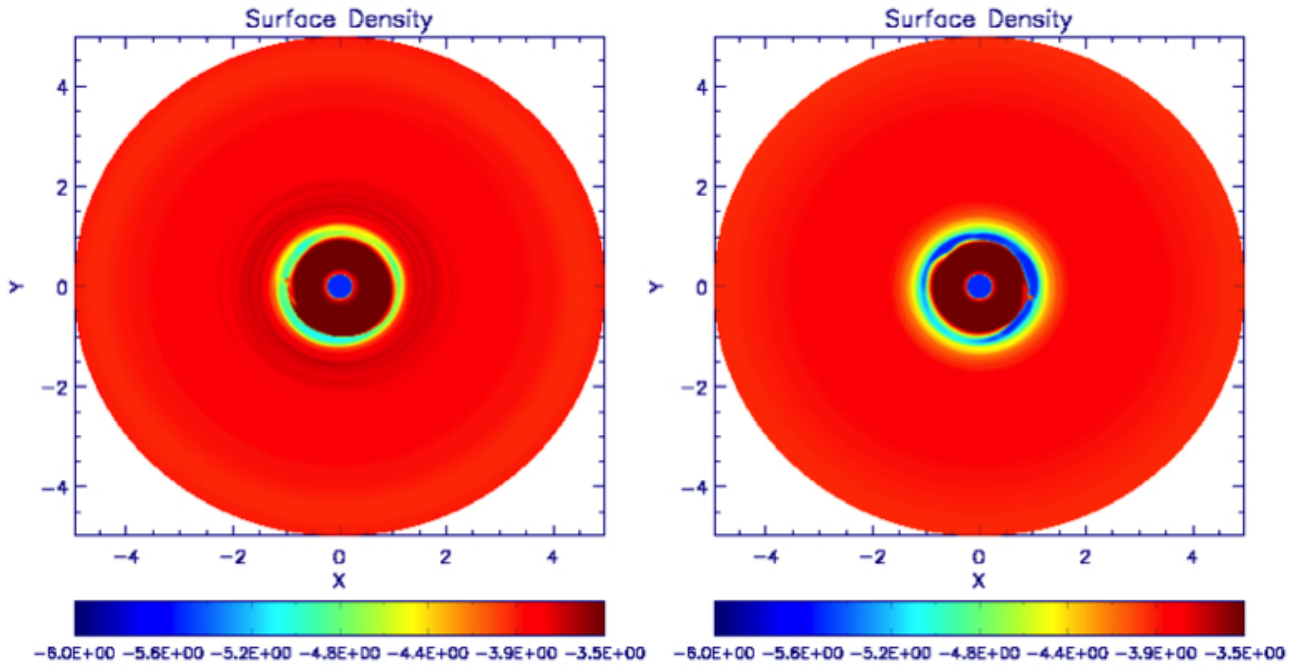

Fig. 8. As in Fig. 7 but for $q = 0.01$ with softening length $0.6H$ after 100 orbits (left panel) and 800 orbits (right panel). As the mass ratio is lower in this case compared to that of Fig. 7 the gap in the disk is narrower. The companion, indicated by a small red circle is found in general to orbit closer to the inner disk edge at earlier times. In the left hand panel the companion grazes the inner edge slightly above the x axis for $x < 0$. This enhances the accretion rate at that stage.

process of gap formation, which is necessary for this time scale to be valid, as well as demonstrated compatibility with the evolution of the accretion disk which supplies the mass flow via material on approximately circular orbits.

10. Estimating the accretion rate onto the secondary

We now give simple estimates for the possible accretion rate onto the perturber in the spirit of our simplified 1D modelling approach. concluding that this is not expected to produce significant effects on orbital evolution. However, it can lead to non-trivial activity and be relevant to studies aimed at the investigation of means of detection of SBBH and other similar systems.

In order to estimate the accretion rate, $\dot{m}$, to the secondary we assume that all gas elements, which approach the secondary within an accretion radius, r_a, are accreted to the secondary. r_a is estimated as in standard Bondi-Hoyle accretion (Bondi & Hoyle 1944), but we take into account the fact that a typical relative velocity of a gas element with respect to the secondary, v_{rel}, is twice of the Keplerian value. Accordingly we obtain $r_a = qr_p/2$. Adopting these assumptions the accretion rate to the secondary, $\dot{m}$, can be easily estimated in two limiting cases $r_a \gg H$ and $r_a \ll H$ [6] as

$$\dot{m}_1 \approx 4r_a H \rho_{min} v_{rel} \quad \dot{m}_2 \approx \pi r_a^2 \rho_{min} v_{rel}, \tag{71}$$

[6] Note that the latter case formally violates the sufficient condition for a 'sufficiently massive' binary (44). Nonetheless we consider it to compare our analytical estimates with the results of numerical simulations, for which the disk is relatively thick, and which marginally corresponds to this case even though q exceeds both q_1 and q_2 so that the binary is in fact 'sufficiently massive'.

where the indices 1 and 2 correspond to the former and latter cases, respectively, $\rho_{min} \approx \Sigma_{min}/(2H)$ and we use the first expression in (59) to estimate Σ_{min}, making the assumption that the softening length is sufficiently small. Using the explicit expressions of all quantities entering (71), we obtain

$$\dot{m}_1 \approx 4\pi q \left(\frac{\Sigma_{min} r_0^2}{P_0}\right) \text{ and } \dot{m}_2 \approx \frac{\pi^2}{2}\frac{q^2}{\delta}\left(\frac{\Sigma_{min} r_0^2}{P_0}\right), \tag{72}$$

where we have assumed for simplicity, that $r_p \sim r_0$.

We now use the estimate of the minimum surface density given by (59) in (72) thus obtaining

$$\dot{m}_1 \approx 2.5\pi q^{1/3} F \nu_0 \Sigma_0, \text{ and } \dot{m}_2 \approx 0.3\pi^2 q^{4/3}\delta^{-1} F \nu_0 \Sigma_0 \tag{73}$$

The expressions (73) can be further simplified for a disk of infinite extent. From the discussion in Section 8.2 it follows that in this case $F \sim 1$ and, accordingly, the accretion rate through the disk $\dot{M} \sim \dot{M}_* = 3\pi\Sigma_0\nu_0$. Therefore, from the first expression in (73) we expect that

$$\dot{m} \approx q^{1/3}\dot{M}, \tag{74}$$

where we have neglect a numerical factor order of unity. It then follows from the expression (70) for the orbital evolution time that the mass of the secondary can only increase by a fraction $q^{1/3}/2$ during significant orbital evolution, even when the disk is very thin. This fraction will be smaller for a thick disk. We remark that in addition, the disk could be thickened locally as a result of radiative processes, producing a back reaction on the accretion flow. Thus accretion is not expected to affect the orbital evolution significantly. It is important to stress that although we have assumed that $r_p \sim r_0$ when deriving (74), this expression is, in fact, valid for any r_p.

11. Numerical simulations of gap formation, migration and accretion onto the perturber

In this section we consider numerical simulations that resulted in gap formation. They were performed for $q = 0.01$ with standard softening, and for $q = 0.02$ and $q = 0.01$ with small softening (see Section 5). For cases with standard softening, the computational domain was taken to be $(0.2r_0, 5r_0)$. For the other cases it was $(0.4r_0, 4r_0)$. Other features of the simulations were as described in Section 5.

11.1. Accretion and migration

Some simulations were performed with the perturber allowed to accrete mass from the disk. Following the approach of Bondi & Hoyle (1944), the accretion rate is then taken to be $\dot{m} = \pi r_a^2 \Sigma v_{rel}/(2H)$ (see equation (71)). In implementing this we removed mass uniformly from the grid cell containing the perturber and its eight nearest neighbours. In this context we remark that in the small softening cases the grid size is approximately equal to, or somewhat less than, both the softening length and the accretion radius. Furthermore tests showed that results in particular for the total amount of mass accreted over long periods of time, were not sensitive to the detailed implementation, not being significantly changed even when the mass was removed only from the grid cell containing the perturber.

To calculate the torque acting on the perturber, contributions arising from gravitational torques from the disk as well as the mass and momentum accreted by the perturber were taken into account. The latter effects were found to play only a minor role for the simulations reported here. As indicated above simulations with $q <\sim 0.003$ did not readily exhibit gap formation, with the perturber remaining in a type I migration regime, at least on time scales of a few hundred orbits, although this picture could potentially be modified on very long time scales through the cumulative dissipation of weak shock waves.

The structure of the disk gaps for $q = 0.02$ and $q = 0.01$ is illustrated in the surface density contour plots presented in Figs. 7 and 8 at various times. The runs illustrated respectively correspond to the strongest and weakest gap forming cases considered in this section. Note that the gap is indeed significantly wider and deeper for $q = 0.02$ as expected and in addition the gap edges define significantly non circular boundaries as mentioned above. Material crossing the gap in the form of streamers is also present. Note that animation of the process of gap formation can be found on website http://astro.qmul.ac.uk/people/sijmejan-paardekooper/publications.

The semi-major axis is shown as a function of time for $q = 0.02$ and $q = 0.01$ for small softening and for $q = 0.01$ with standard softening in Fig. 9. The behaviour depends only very weakly on whether the perturber is allowed to accrete from the disk or not. At early times the cases with $q = 0.01$ have the migration rates expected in the type I regime (see Fig. 9) being approximately $\propto \Delta_s^{-1}$ in agreement with the discussion in section (5.1) above. However, after a few orbits the effects of gap formation become noticeable and the migration starts to slow down. For the case with $q = 0.02$ the initial migration rate is a factor of two smaller than the expected type I migration rate with the effects of gap formation being noticeable immediately. Note that at longer times the migration rates for $q = 0.01$ with

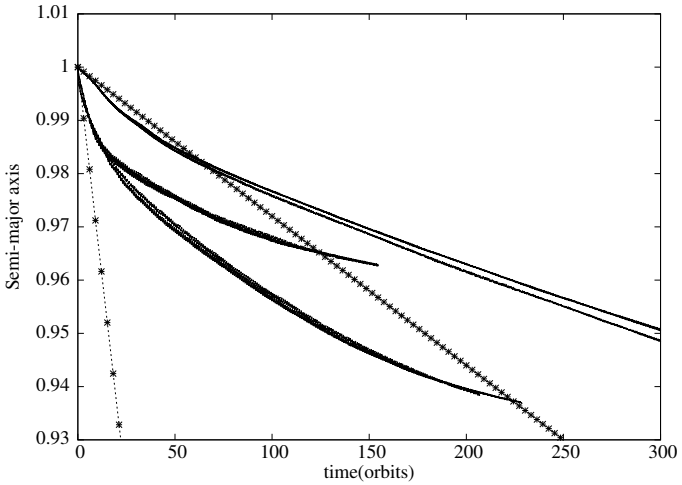

Fig. 9. Semi-major axis, in units of the initial orbital radius, as a function of time for $q = 0.02$ and $q = 0.01$ for small softening and for $q = 0.01$ with standard softening. Two curves without imposed crosses, which are very close together, are shown for each of these three cases. The uppermost pair of curves corresponds to $q = 0.01$ with standard softening and the lowermost pair for $q = 0.01$ with small softening. The central pair corresponds to $q = 0.02$ with small softening. The lower of the pair of curves for the cases with small softening correspond to runs with accretion from the disk included (see text). For the case with standard softening this situation is reversed. The straight lines with imposed crosses is obtained by adopting the initial type I migration rate with contributions from all $m \leq 100$ included. The line with the more widely separated crosses corresponds to $q = 0.01$ with small softening while the other line corresponds to $q = 0.01$ with standard softening.

different softening lengths slow to become approximately equal as would be expected if the migration was governed by the viscous evolution of the disk. There was a deeper and wider gap in the small softening case, the ultimate migration being somewhat slower. This might be expected on account of the wave excitation and associated angular momentum removal being apparently more effective in the case with standard softening.

On the other hand, the larger open inner boundary radius adopted for the simulations with smaller softening, on account of necessary numerical convenience, results in a relatively larger angular momentum loss as material passes through it.

This not available to the secondary mass resulting in an expected slowing of the the inward migration rate as compared to simulations with a smaller inner boundary radius (see discussion in section 8 below). The case with $q = 0.02$ ends with slowest migration rate as expected. In all cases the characteristic time scale becomes comparable to or greater than that for the viscous evolution of the disk. To consider this issue more precisely a comparison between the orbital evolution obtained from some of these simulations and the semi-analytic model for which the orbital evolution is driven by the viscous evolution of the disk is given in section 9.

Accretion onto the secondary from the disk plays only a minor role in these simulations as illustrated in Fig. 10. We remark that the accretion rate can show large variations

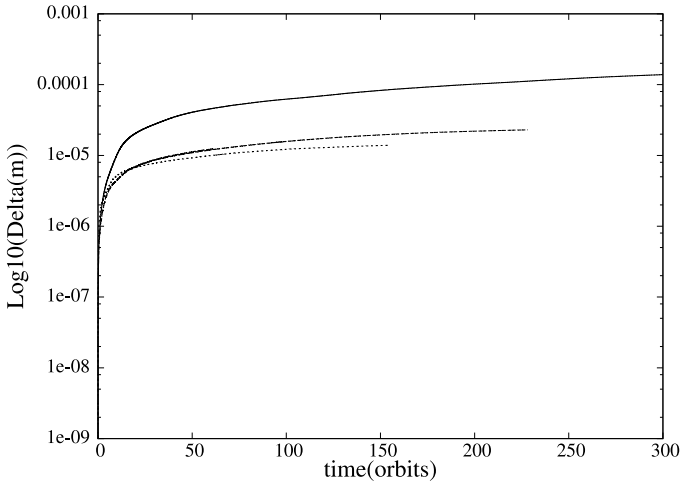

Fig. 10. The mass accreted, in units of M, as a function of time for runs with accretion illustrated in Fig. 9. The uppermost curve corresponds to $q = 0.01$ with standard softening, the central curve to $q = 0.01$ with small softening and the lowermost curve corresponds to $q = 0.02$ with small softening. Note that although the accretion rate shows large variations, these curves do not because they effectively time average this quantity.

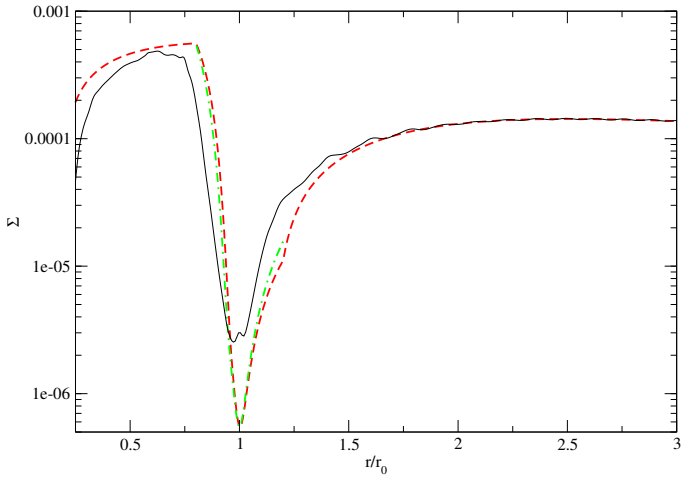

Fig. 11. The surface density Σ in units M/r_0^2 is shown as a function of the radial coordinate, for the moment of time corresponding to $t = 1500P_0$. The perturber was initiated in the disk at $t = 0$. The solid curve is obtained from a direct two dimensional simulation and averaging over the azimuthal coordinate. The dashed curve is obtained from a numerical solution of equation (34) and the dot dashed curve gives the shape of the gap according to equation (47) with the constants F and C_- obtained from a fit to the numerical solution of (34), see the text for more details.

on an orbital time scale. These are due to the disk edges not being circular enabling the secondary to approach, in particular the inner disk edge, where the accretion rate naturally increases, quasi-periodically on an orbital time scale. In spite of this it is found that the time averaged accretion rate is well behaved and significantly slower for cases with wider and deeper gaps as expected. This is discussed further in section 11.3 below. For the simulations presented here the accretion rate is never large enough to double the perturber's mass on its migration time scale.

11.2. Comparison of analytical and numerical results on the gap profile

We compare results of a numerical simulation of the type described in Section 11 with results obtained from the numerical solution of equation (34) within the framework of the simplified one-dimensional model and also with an analytic surface density profile obtained (49) in Fig. 11. The simulation adopted corresponds to the case with the mass ratio $q = 10^{-2}$ and standard softening described in Section 11. The initial surface density profile was taken to be $\Sigma = \Sigma_0(r/r_0)^{-1/2}$ which corresponds to $F_0 = 0$ in equations (39) and (40). The value $\Sigma_0 = 2.4 \times 10^{-4} M/r_0^2$ was adopted to correspond to the numerical simulation.

In Fig. 11 the surface density Σ is shown as a function of r/r_0 for $t = 1500P_0$, we recall that $P_0 = 2\pi\sqrt{r_0^3/GM}$. Note that we determine the constants F and C_- in (49) using the solution obtained with help of our one-dimensional numerical approach, by matching the values of mass flux through the gap and a value of the surface density at the inner edge of the gap. We see from Fig. 11 that the profiles of Σ given by the analytical expression (49) and the numerical solution of equation (34) almost coincide. There is also a good agreement between the surface density profiles obtained from these approaches and those obtained from two dimensional numerical simulations apart from the region

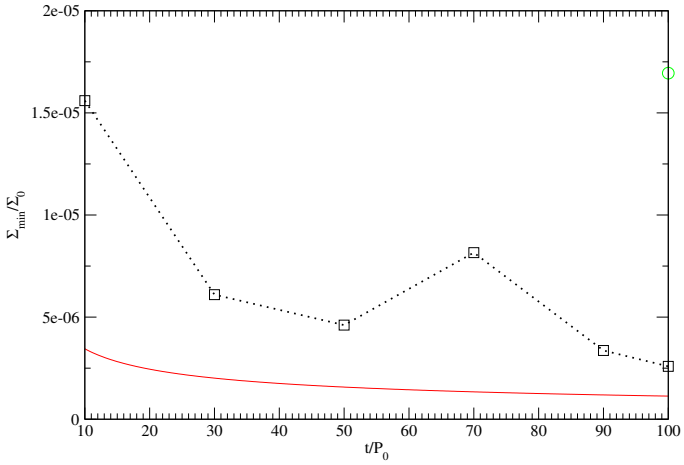

Fig. 12. The minimal value of surface density Σ_{min} in the gap in units of initial surface density $\Sigma_0 = 2 \cdot 10^{-4} M/r_0^2$ is shown as a function of the dimensionless time t/P_0. Squares connected by the dotted line represent the result of two-dimensional numerical calculations while the solid curve is calculated according to the first expression (59).

very close to the surface density minimum, In this region the two dimensional simulations give values of Σ roughly five times larger than the other approaches. This can be explained by having adopted an oversimplified treatment of the angular momentum exchange within the framework of the impulsive approximation. Also note that the estimate of the minimum surface density based on equation (59) gives practically the same values as that obtained from (49), and, therefore, is not shown.

In that context in Fig. 12 we compare numerical simulation results for the minimum surface density in the gap with the expression (59). The parameters of the numerical

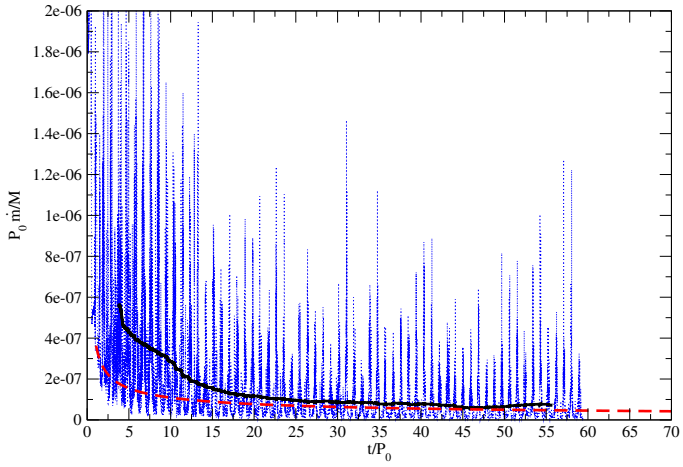

Fig. 13. The accretion rate onto the secondary in units M/P_0 as a function of time. The dotted curve, showing large variations, is obtained numerically, the solid curve represents the numerical results time averaged over 7.5 periods, while the dashed curve represents $\dot{m}_2$ as specified through one of the equations (73).

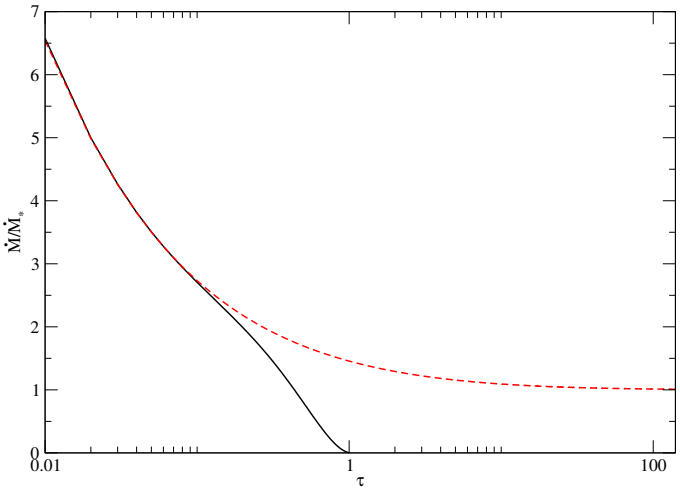

Fig. 14. The dimensionless mass flux $\dot{M}/\dot{M}_*$ is shown as a function of time τ for the case $a = 2/3$, $b = 1$ (model 1). The solid curve corresponds to our model of the disk of finite size. The dashed curve shows, for comparison, the same dependence for the disk of formally infinite extent.

simulation we consider are the same as described above except that the mass ratio is $q = 2 \cdot 10^{-2}$ and $\tilde{\Delta}_s = 5 \cdot 10^{-3}$. The value of the dimensionless flux F entering (59) is calculated as outlined in Appendix A. As seen from Fig. 12, apart from the at the times $t = 10P_0$ and $t = 70P_0$, where the analytical results give much smaller value of Σ_{min}, the analytical and numerical results are in reasonable agreement with the numerical results giving $2 - 3$ times larger values of Σ_{min} as indicated in section 7.1.1.

11.3. Comparison of the analytic estimate of the accretion rate with the results of a simulation

We consider the run with $q = 2 \cdot 10^{-2}$ and $\delta = 0.05$ described in section 11. A comparison of the accretion rate measured in the numerical simulation with our analytical estimate is shown in Fig. 13. Since in this case $r_a < h$ we use the second expression in (73) to make the comparison. The numerical data (dotted curve) shows sharp variations of the accretion rate. These variations are due to the secondary approaching the inner disk edge where the surface density is larger. Such approaches can occur because the inner disk edge is not circular and they repeat approximately periodically on the orbital time scale. This effect may have important observational consequences since it may lead to variation of the secondary luminosity.

When the numerical data is averaged over time intervals of 7.5 orbital periods there is a good agreement between both approaches with the analytical curve giving somewhat smaller values of $\dot{m}$. This may be due to the fact that our analytical expression for Σ_{min} underestimates the minimum values of the azimuthally averaged surface density in the gap that is found in simulations. But note that the accretion rate can reach values an order of magnitude larger than the locally averaged value.

11.4. A comparison of semi-analytic models and numerical simulations of migration in an accretion disk of finite extent in which a gap forms

Here we compare orbital migration determined using equations (6), (7) and (62) together with (63) (see Section 9) with results of numerical simulations. We performed several two dimensional numerical simulations of accretion disks of finite radial extent, $0.25 \leq r/r_0 \leq 5$. We remark that for these disks the dependence of $\dot{M}$ on t differs from that appropriate to the case of a disk of formally infinite extent. In this case, a slightly different calculation of the dependence of $\dot{M}(t)$ needs to be undertaken to compare with the orbital evolution obtained from simulations.

Here we make a comparison for a sufficiently large mass ratio, $q = 10^{-2}$, and two disk models. Model 1 employed the non-linear viscosity law with $a = 2/3$, $b = 1$ and the initial surface density profile corresponding to zero angular momentum flux through the disk , i. e. given by equation (39) with $F_0 = 1$. Model 2 adopted a constant viscosity for which $a = b = 0$, and the initial surface density profile as for Model 1. In both cases the dimensionless viscosity coefficient $\nu_0 = 10^{-5}$, $\delta = 0.05$, we adopted standard softening and the initial disk mass, $M_d = 3 \times 10^{-3} M$.

For model 1 we solve equation (63) numerically, and use equations (6), (7), (62) and the definition of $\dot{M}_*$ to find the dependence of r_p on time. The dimensionless mass flux for this model is shown in Fig. 14 as a function of time τ and the binary separation distance as a function of t/P_0 is shown in Fig. 15 together with the results obtained from the two dimensional numerical simulation. One can see that both approaches give excellent agreement. The result based on the solution of (63) also predicts that eventually the evolution stalls, since on account of its being finite, all the disk mass is eventually accreted by the primary in this model.

For model 2 we develop an analytic approach to the calculation of the evolution of r_p in Appendix A. The result is given by equation (A.13) and is compared with a two dimensional simulation in Fig. 16. As for the non-linear

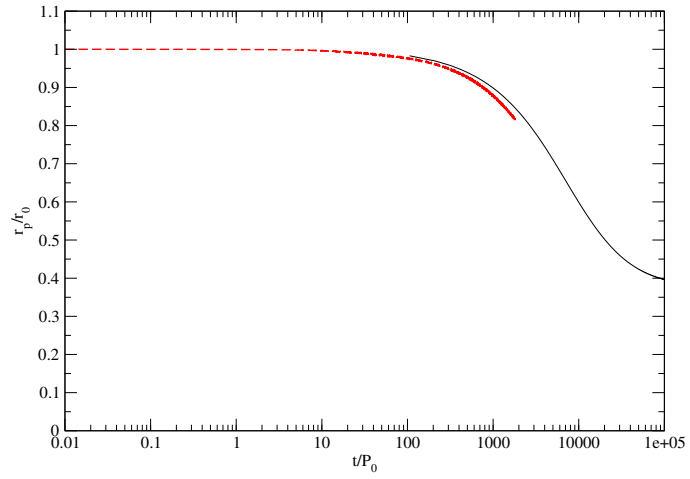

Fig. 15. The dependence of the binary separation distance, r_p/r_0, as a function of t/P_0 for model 2. We recall that r_0 and P_0 are the binary separation distance and orbital period at the initial time $t = 0$. The solid curve is obtained from the solution of equation (63) while the dashed curve represents the results of a two dimensional numerical simulation.

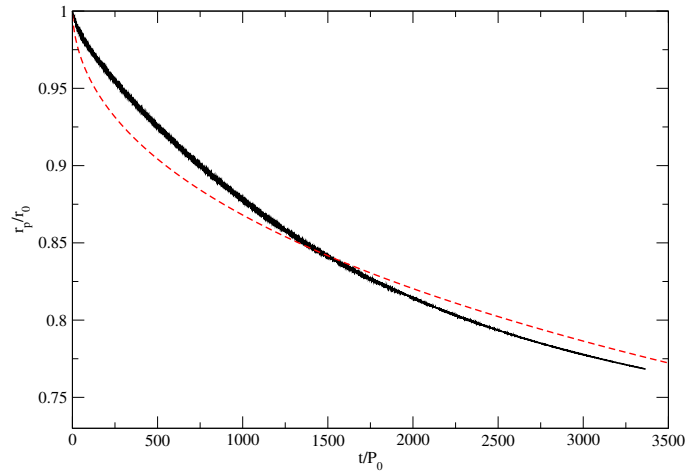

Fig. 16. The dependence of the binary separation distance on time. The solid curve shows the result of numerical simulation with the mass ratio $q = 10^{-2}$ and other parameters described in the text, the dashed curve is calculated from equation (A.13).

case we have again a very good agreement between the numerical and analytical approaches.

12. Discussion

In this Paper we have studied the evolution of a secondary mass embedded in an accretion disk in a quasi-circular retrograde orbit. Before summarising our conclusions we briefly discuss some additional phenomena and processes that may be important under some circumstances. We consider effects that could occur if the binary orbit possessed a moderate to large eccentricity and the importance of orbital evolution arising from the radiation of gravitational waves for perturbers orbiting close to the central mass.

Additional phenomena and processes

12.1. A binary with large orbital eccentricity

A binary black hole may have a large eccentricity at the stage when interaction with the disk becomes important, (see e.g. Polnarev & Rees 1994). In other potential astrophysical applications of the scenario considered in the Paper, for example to exoplanetary systems, a massive planet can, in principal, have its direction of orbital motion opposite to that of the protoplanetary disk, only as a result of its gravitation interaction with other objects. In this case, large eccentricities would also be expected. Perhaps, the most important qualitative difference between the case of an eccentric binary and the case of circular binary considered in this Paper, is that in the former case, outer Lindblad resonances are still possible, though with amplitudes significantly reduced in comparison to the prograde case. Contrary to the impulsive and non-resonant torques considered in this Paper the Lindblad torques are necessarily positive with respect to the direction of gas motion, see e.g. Goldreich & Tremaine (1979). Thus, if a disk is sufficiently thin, there is a possibility of gap formation in the 'standard sense' with the disk gas being repelled from the binary orbit radii as the result of an outward flux of positive angular momentum supplied by waves launched at the resonances. Let us briefly consider this possibility and estimate typical disk parameters for which a gap could be opened, assuming that the binary has an eccentricity $e \sim 1$.

We use the standard expressions for the resonant torques, T_{ml}, associated with perturbations with a particular azimuthal mode number, m, and a particular time harmonic number l using expressions from Artymowicz & Lubow (1994), hereafter AL, for the corresponding component of the gravitational potential due to the perturber assuming that the binary mean motion, or orbital angular velocity, ω, entering these expressions is negative. Then, terms with negative values of l correspond to waves propagating in the direction of the disk's rotation. It is readily found (see e.g. AL) that the torques T_{ml} scale approximately as $e^{2|m-l|}$ in the limit of small eccentricities. Therefore, we parametrise them through the expression

$$T_{ml} = \tau_{ml} q^2 e^{2|m-l|} \Sigma (GMa), \qquad (75)$$

where a is the semi-major axis which is clearly such that $a = r_p$ when $e = 0$.

The most important torques T_{ml} are those corresponding to the smallest difference $|m - l|$ with $l < 0.$, i.e. terms with $m = 1$ and $l = -1$, $m = 2$ and $l = -1$ and so on. Assuming that e is small one can use expressions in AL to obtain

$$\tau_{(1,-1)} \approx 0.69, \quad \tau_{(2,-1)} \approx 0.57, \qquad (76)$$

and the corresponding resonances reside at radii

$$r_{(1,-1)} = 4^{1/3} a, \quad r_{(2,-1)} = 3^{2/3} a. \qquad (77)$$

A general dependence of these quantities on e can be obtained numerically. This is shown in Fig. 17 together with a corresponding calculation with $m = 2, l = 1$ evaluated for a prograde orbit, which is shown for comparison.

As indicated by Fig. 17 the asymptotic expressions (76) are approximately valid even in case of rather large eccentricities. In particular, the numerical factor in the $(1, -1)$ term changes from 0.69 to 0.76 when e grows from zero to its

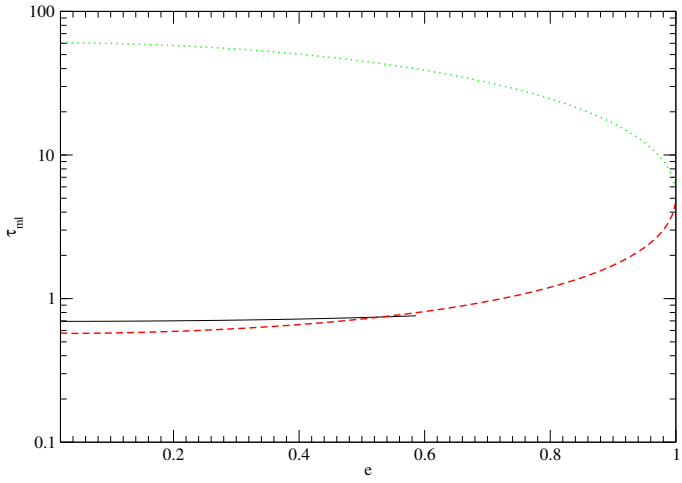

Fig. 17. The dimensionless torques τ_{ml} are shown for the cases $m = 1, l = -1$ (solid curve), $m = 2, l = -1$ (dashed curve) and $m = 2, l = 1$ (dotted curve) as functions of eccentricity e. Note that the solid curve ends at $e = 0.58$. At this value of eccentricity, the apocentre distance $r_p = a(1 + e)$ is equal to $r_{(1,-1)}$ given by equation (77). At larger values of e the corresponding resonance lies within the binary orbit. Also note that the case $m = 2, l = 1$ shown for illustration corresponds to prograde orbital motion of the binary.

maximal value ≈ 0.58 corresponding to the position of the resonance situated at the apocentre distance. Analogously, the numerical factor of the $(2, -1)$ term is smaller than unity for eccentricities smaller than 0.72. Thus, the expressions (76) can be used for estimates of the corresponding torques at moderate values of eccentricity. Accordingly we use expressions for our estimates of conditions for gap formation below.

In order to proceed we use the criterion proposed in Lin & Papaloizou (1979b), see also AL. Namely, we assume that a gap can be opened provided the angular momentum flux due to viscous forces, $\dot{L}_* = 3\pi\Sigma\nu\Omega r^2 < T_{ml}$. Note that $\dot{L}_*$ is evaluated at $r = r_{(m,l)}$. Using this condition, equations (37), (75), and assuming that α and δ are small, we obtain a condition for gap formation in the form

$$e > e_{crit}^{ml} = \left(\frac{3\pi\alpha\delta^2 r_{m,l}}{\tau_{ml} q^2 a} \right)^{1/(2|m-l|)} . \qquad (78)$$

Now we use (76) and (77) to obtain

$$e_{crit}^{1,-1} \approx 0.2 \alpha_*^{1/4} q_*^{-1/2} \delta_*^{1/2} \qquad (79)$$

and

$$e_{crit}^{2,-1} = 0.37 \alpha_*^{1/6} q_*^{-1/3} \delta_*^{1/3} \qquad (80)$$

for $m = 1$, $l = -1$ and $m = 2$, $l = -1$, respectively, where $\alpha_* = \alpha/10^{-2}$, $q_* = q/10^{-2}$ and $\delta_* = \delta/10^{-3}$.

Since the critical eccentricities are of the order of $0.2 - 0.4$ for very thin accretion disks, which may be present in galactic nuclei, this effect may operate there. The situation is less favourable for protoplanetary disks, where we typically have $\delta \sim 0.05$, and, accordingly, $\delta_* \sim 50$. In this case we have the critical eccentricities formally exceeding unity for $\alpha_* = 1$, and, therefore, this effect is unlikely to operate unless α is very small.

We comment that the gap opening process considered here differs from that considered in previous sections for near circular orbits for which the disk edges are relatively close to the perturber. For the case of a perturber in an eccentric orbit considered here, the gap is maintained by interactions at Lindblad resonances such that the outer disk edge may be a distance of order a even from apocentre. Angular momentum transfer to the perturber from material streaming through the cavity due to viscous evolution of the disk may occur and also contribute to the maintenance of the gap. However, on account of a gap being produced through their action, Lindblad torques are at least comparable to viscous torques. Accordingly angular momentum exchange with the perturber due to Lindblad torques and streaming material are potentially comparable.

If the gap opening by Lindblad resonances can indeed be realised and these are important for the angular momentum exchange, the binary evolution would be quite different from that described in this Paper. It may be closer to the regime discussed by IPP. Note, however, that non-resonant effects may interfere with gap formation due to resonances when apocentre approaches the radius of a resonance.

Also, note that when resonances give the main contribution in the energy and angular momentum exchange between the binary and the disk, the binary eccentricity decreases with time, and, therefore, the gap can be eventually overrun by the disk gas, after which, the evolution will proceed in a manner similar to that discussed in this Paper[7]. The effects discussed above are in need of further investigation.

In this context we comment that the evolution of massive binary immersed in a circumbinary disk is also potentially interesting in the context of disk-planet interactions (see e.g. Papaloizou et al. 2007) for a review. Although it is generally accepted that the planets are formed in the protoplanetary disk rotating in the prograde sense, a gravitational interaction between a group of planets (see e.g. Rasio & Ford 1996, Papaloizou & Terquem 2001) may, in principle, lead to the formation of a planetary orbit of high eccentricity with the direction of orbital rotation opposite to that of a disk of finite extent and which enters into it. Physically, this may be achieved by different generalisations of the well-known Lidov-Kozai effect, see e.g. Ziglin (1975), Farago & Laskar (2010), Katz, Subo & Malhotra (2011) and Li et al. (2013).

12.2. The influence of emission of gravitational waves on the orbital evolution and accretion rate for SBBH

In the case of SBBH there is an additional important mechanism for driving orbital evolution through emission of gravitational waves. For a circular orbit and $q \ll 1$, the corresponding time scale can be easily obtained from expressions given by e.g. Landau & Lifshitz (1975) as

$$t_{gw} = \frac{5 r_g}{8 c q} \left(\frac{r_p}{r_g} \right)^4 , \qquad (81)$$

where $r_q = 2GM/c^2 \approx 3 \cdot 10^{13} M_8 cm$, with $M_8 = M/10^8 M_\odot$, and c denoting the speed of light from now on.

[7] Let us also remark that SPH simulations with a large mass ratio, $q = 1$, indicate that when the eccentricity is sufficiently large, the inclination angle between the binary and the disk may grow with time, see Roedig & Sesana (2014).

From equation (70) it follows that the time scale for orbital evolution due to interaction with the disk can be written in the form

$$t_{ev} \approx 5 \cdot 10^7 \left(\frac{q_{-2} M_8}{\dot{M}_{-2}} \right) yr, \quad (82)$$

where $q_{-2} = q/10^{-2}$ and $\dot{M}_{-2} = \dot{M}/(10^{-2} M_\odot yr^{-1})$. From the condition $t_{gw} < t_{ev}$ we conclude that gravitational waves will determine the orbital evolution when

$$r_p < r_{gw(I)} = r_g \left(\frac{8cqt_{ev}}{5r_g} \right)^{1/4} \approx \frac{0.7 q_{-2} M_8}{(\dot{M}_{-2})^{1/4}} \ pc. \quad (83)$$

Note that the orbital period at $r_p \sim r_{gw(I)}$ being given by $P_{orb} \approx 5 r_{-2}^{3/2} M_8^{-1/2} yr$, where $r_{-2} = r_p/(10^{-2} pc)$ is expected to be of the order of a few years. From the definition of $r_{gw(I)}$ and (81) it also follows that

$$t_{gw} = \left(\frac{r_p}{r_{gw(I)}} \right)^4 t_{ev}. \quad (84)$$

Another important scale, $r_{gw(\nu)}$, is determined by the condition that the time scale for orbital evolution due to gravitational radiation be less than the time scale for viscous evolution of the disk, or $t_{gw}(r_p < r_{gw(\nu)}) < t_\nu$. Making use of (37) we obtain

$$r_{gw(\nu)} = r_g \left[\frac{32\sqrt{2} q}{15 \alpha \delta^2} \right]^{2/5} \approx 5 \cdot 10^{-3} M_8 (q_{-2})^{2/5} \alpha_*^{-2/5} \delta_*^{-4/5} pc. \quad (85)$$

When $r < r_{gw(\nu)}$ the absolute value of the radial velocity of the perturber exceeds that of the disk gas. In this regime the disk gas is transferred from the inner part of the disk to the outer part opposite to the regime considered above. However, arguments leading to the expression (74) remain essentially the same if instead of the accretion rate through the disk, $\dot{M}$, the rate of transfer of the disk gas through perturber's orbit, $\dot{M}_{tr}$, is used. Note that $\dot{M}_{tr}$ is defined in the frame, where perturber is at rest. We can estimate it as $\dot{M}_{tr} \sim M_d(r < r_p)/t_{gw}$, where the disk mass inside the perturber's orbit can be found from the first expression of (60). On the other hand, as discussed above the disk inside the perturber's orbit may be approximated as a stationary disk characterised by the accretion rate $\dot{M}$, and, therefore, its mass can be estimated as $M_d(r < r_p) \sim \dot{M} t_\nu$. Taking these considerations into account we obtain

$$\dot{m} \sim \frac{q^{1/3} M_d(r < r_p)}{t_{gw}} \sim \frac{q^{1/3} \dot{M} t_\nu}{t_{gw}} \sim \frac{q^{1/3} \dot{M} r_{gw(\nu)}^4}{r^4}. \quad (86)$$

This indicates that the accretion rate onto the secondary can exceed that onto the primary, $\sim \dot{M}$, provided that

$$r < r_{crit} = q^{1/12} r_{gw(\nu)}. \quad (87)$$

Since the power of q in (87) is small, we have that typically $r_{crit} \sim r_{gw(\nu)}$. Note, however, that even when $r < r_{crit}$ the luminosity of the secondary does not necessarily exceed that of the primary. This is also determined whether the mode of accretion onto the secondary is disk-like or more approximately spherical. This issue is one for future investigation.

12.3. Secular evolution of directions of angular momenta of the binary and the disk

As mentioned in Introduction the gravitational torque exerted by a stationary twisted circumbinary disk on the binary orbit changes its orientation on a long timescale t_{or}. It is assumed that the disk is aligned with the binary orbital plane at scales smaller than the alignement radius r_{al}, but misaligned at scales r_{al} with some inclination angle, which may be initially small but subsequently may become large enough for non-linear effects to become important. The action of the disk torque tends to overturn the binary orbit when it is retrograde, see e.g. IPP.

When the inclination angle is large enough non-linear effects are important, and for an estimate of the time t_{or}, we formally assume that the effective α for the twisted disk ~ 1, see e.g. Ogilvie (1999) for a theoretical justification and also Lodato & Price (2010) for numerical SPH simulations of the evolution of twisted disks in the regime of large gradients of the disk's tilt. [8] We then use the simple estimate of t_{or} given in IPP as

$$t_{or} \sim \sqrt{\frac{r_p}{r_{al}}} \frac{M_p}{\dot{M}}, \quad (88)$$

where the alignement radius $r_{al} \sim r_p \sqrt{q}/\delta$ (see equation (23) of IPP). Recalling that the orbital evolution timescale $t_{ev} = M_p/(2\dot{M})$ we get

$$t_{or} \sim 0.2 \delta_*^{1/2} q_*^{-1/4} t_{ev}. \quad (89)$$

Note that although the numerical factor in (89) is clearly approximate, it would increase if a smaller value of the effective α had been used as long as it exceeded δ. One sees that as long as $r_{al} \sim r_p$, as is the case for the gap forming simulations discussed in Section 11, $t_{or} \sim t_{ev}$, which occurs because the process inducing inclination changes works at the same rate as that producing changes to the semi-major axis. In that case changes in the orientation of the orbit may not be significant. On the other hand, for some values of q and δ, r_{al} could exceed r_p significantly enough that the timescale for the orientation evolution could be somewhat smaller than the orbital evolution timescale leading to significant changes in inclination. This is an aspect for future study.

13. Summary of results and conclusions

In this Paper we have considered a binary with small mass ratio $q \ll 1$ embedded in an accretion disk with the direction of orbital motion being retrograde with respect to the rotation of the disk. We studied the evolution of the semi-major axis and the mass accretion rate onto the secondary component focusing on the case of a quasi- circular orbit.

[8] Note that there are non linear effects operating in twisted disks with finite inclination angles, which are not considered in Ogilvie (1999), such as a possibility of standing shocks, see e.g. Fragile & Blaes (2008). These effects could lead to additional damping of non-stationary twisted disturbances once the inclination to the binary orbit exceeds $\sim \delta$, see e.g. Sorathia et al. (2013), and may act so as to produce an increase of the effective α. Also, the presence of shocks may increase the disk thickness since they provide an additional source of energy dissipation.

We employed several approaches to the problem. A simple semi-analytic approach based on solving a one dimensional diffusion equation for the disk surface density that incorporated a local scattering model for estimating the rate of angular momentum exchange between the orbit and disk, which resulted in evolution of the orbit. In addition to this we presented a simplified purely analytic calculation of the surface density profile in the vicinity of the perturber and the construction of a similarity solution for the outer disk that was applicable when the latter was of infinite extent. Under the assumption of slow orbit evolution, valid when the secondary mass is much larger than the local disk mass, the rate of orbital evolution in the form of an inward migration could be readily calculated. In addition to these approaches we performed two-dimensional numerical hydrodynamical simulations. All methods were found to be in qualitative, and often, as in the context of orbital semi-major axis evolution, in quantitative agreement.

We found that for binaries with very small mass ratios, the secondary component migrated through the disk leaving the surface density virtually unchanged. This corresponds to the usual type I migration regime for prograde orbits. The orbital evolution is due to the launching of tightly wound density waves that propagate away from the orbit (see section 4). We calculate the evolution rate, which is much less than in the prograde case,

When the mass ratio is sufficiently large, $q >\sim 1.57\delta^2$, $\sim 10^{-3} - 10^{-2}$, for typical parameters considered, a gap in the disk opens in the vicinity of the perturber's orbit (see sections 6.4 and 11). However, the form of the gap and the way it opens are not the same as in the prograde case. In the retrograde case gap opening is produced by efficient removal of angular momentum in the vicinity of the orbit as the disk material passes through it. This leads to a depression of the surface density profile near the orbit that we are able to match quite well using simplified analytic modelling.

Provided that the secondary mass is significantly larger than the typical disk mass in the vicinity of its orbit, the disk exterior to the gap over a length scale of order r_p relaxes to a quasi-stationary state characterised by the rate of mass flow through the disc, $\dot{M}$, on a time scale that is characteristic of the local viscous time scale, but significantly shorter than the characteristic time scale of orbital evolution, t_{ev}. For a disk of large radial extent $\dot{M}$ is comparable to the accretion rate at large distances. The orbital evolution time scale, t_{ev}, was found to be of $M_p/(2\dot{M})$, where M_p is the secondary mass (see section 9).

When the orbital evolution is solely determined by interaction with the disk, the time averaged accretion rate onto the secondary, $\dot{m}$, is estimated to be at most $\dot{m} \sim q^{1/3}\dot{M}$, being significantly smaller than the accretion rate onto the primary $\sim \dot{M}$ (see section 10). This behaviour is different from what is seen in the prograde case, where the accretion rates can be reduced due to the presence of a deep cavity in the disk on scales $\sim r_p$. Our numerical results also show large variations of the accretion rate on the orbital timescale. If the radiative efficiency of the accretion onto the secondary is sufficiently large, the binary may manifest itself as a non-stationary source of radiation with typical time scale for variability on the order of the orbital period. It may also be observed as two nearby sources of radiation being blueshifted and redshifted with respect to each other.

In the case of a supermassive binary black hole the orbital evolution is also significantly influenced by emission of gravitational waves. This effect becomes more important than the interaction with the disk when $r_p < 10^{-2}pc$, for typical parameters of the problem. When the evolution is governed by gravitational wave emission such that its inward radial drift speed exceeds the gas radial velocity induced by disk viscosity, it is expected that the accretion rate onto the perturber would increase, possibly becoming larger than $\dot{M}$ for a brief period of time (see section 12.2). Another open issue for future study is a behaviour of the system when the orbit has an appreciable eccentricity. We indicated in section 12.1 that when the binary is very eccentric and the disc is very thin, a conventional gap may be opened due to the effect Lindblad resonances, which are present in this case even for binaries with retrograde orbital motion relative to the disk. In addition to a systematic detailed study of effects arising from orbital eccentricity, another issue for future consideration, is the influence of a mutual inclination of the binary orbital plane with respect to the disk mid plane and the effect of secular evolution of the binary inclination with respect to the disk plane at large distances.

Acknowledgements

We are grateful to R. R. Rafikov, V. V. Sidorenko and the referee for useful comments.
PBI was supported in part by programme 22 of the Russian Academy of Sciences and in part by the Grant of the President of the Russian Federation for Support of Leading Scientific Schools of the Russian Federation NSh-4235.2014.2.

References

Amaro-Seoane, P., Aoudia, S., Babak, S. , et al. , 2013, GWN, 6, 4
Armitage, P. J., Natarajan, P., 2002, ApJ, 567L, 9
Artymowicz, P., Lubow, S. H., 1994, ApJ, 421, 651
Begelman, M. C., Blandford, R. D., Rees, M. J., 1980, Nature, 287, 307
Bogdanovic, T., Smith, B. D., Sigurdsson, S., Eracleous, M., 2008, ApJS, 174, 455
Bogdanovic, T., Eracleous, M., Sigurdsson, S., 2009, New Astronomy, 53, 113
Bondi, H., Hoyle, F., 1944, MNRAS, 104, 273
Burke-Spolaor, S., 2013, CQGRA, 30, 4013
Corsini, E.M. 2014, in Counter-Rotation in Disk Galaxies, ASP Conference Series, Vol. 486, Eds. E. Iodice & E. M. Corsini (ASP: San Francisco), p. 51
Cuadra, J., Armitage, P. J., Alexander, R. D., Begelman, M. C., 2009, MNRAS, 393, 1423
Farago, F., Laskar, J., 2010, MNRAS, 401, 1189
Farris, B. D., Liu, Y. T., Shapiro, S. L., 2011, Phys. Rev. D., 84, 4024
Farris, B. D., Duffell, P., MacFadyen, A. I., Haiman, Z., 2014, ApJ, 783, 73
Fragile, P. C., Blaes, O. M., 2008, ApJ, 687, 757
Grishchuk, L. P., Lipunov, V. M., Postnov, K. A., Prokhorov, M. E., Sathyaprakash, B. S., 2001, Physics Uspekhi, 44, 1
Gold, R., Paschalidis, V., Etienne, Z. B., Shapiro, S. L., Pfeiffer, H. P., 2014, Phys. Rev. D., 89, 4060
Goldreich, P., Tremaine, S., 1979, ApJ, 233, 857
Gould, A., Rix, H.-W., 2000, ApJ, 532L, 29
Haiman, Kocsis, B., Menou, K., 2009, ApJ, 700, 1952
Hayasaki, K., Saito, H., Mineshige, S., 2013, PASJ, 65, 86
Ivanov, P. B., Igumenshchev, I. V., Novikov, I. D., 1998, ApJ, 507, 131
Ivanov, P. B., Papaloizou, J. C. B., Polnarev, A. G., 1999, MNRAS, 307, 79

Ju, W., Greene, J. E., Rafikov, R. R., Bickerton, S. J., Badenes, C., 2013, ApJ, 777, 44
Katz, B., Dong, S., Malhotra, R., 2010, Phys. Rev. Lett., 107, 1101
King, A. R., Lubow, S. H., Ogilvie, G. I., Pringle, J. E., 2005, MNRAS, 363, 49
Kocsis, B., Haiman, Z., Loeb, A., 2012, MNRAS, 427, 2680
Komberg, B. V., 1968, Soviet Astronomy, 11, 727
Komossa, S., 2006, Memorie della Societa Astronomica Italiana, 77, 733
Landau, L. D., Lifshitz, E. M., 1975, The Classical Theory of Fields. Vol. 2, 4th ed., Butterworth-Heinemann
Li, G., Naoz, S., Kocsis, B., Loeb, A., 2013, ApJ, 785, 116
Lin, D. N. C., Papaloizou, J., 1979, MNRAS, 186, 799
Lin, D. N. C., Papaloizou, J., 1979, MNRAS, 188, 191 (b)
Lin, D. N. C., Papaloizou, J., 1986, ApJ, 309, 846
Lin, D. N. C., Papaloizou, J. C. B., 1993, in: Protostars and planets III (A93-42937 17-90), p. 749-835
Liu, F. K., 2004, MNRAS, 347, 1357
Lodato, G. Nayakshin, S., King, A. R., Pringle, J. E., MNRAS, 2009, 398, 1392
Lodato, G., Price, D. J., MNRAS, 2010, 405, 1212
Loeb, A., 2007, Phys. Rev. Lett., 99, 1103
Lobanov, A. P., Roland, J., 2005, A&A, 431, 831
Lynden-Bell, D., Pringle, J. E., 1974, MNRAS, 168, 603
Lyubarskiy, Y. E., Shakura, N. I., 1987, Soviet Astronomy Letters, 13, 386
MacFadyen, A. L., Milosavljevic, M., 2008, ApJ, 672, 83
McKernan, B., Ford, K. E. S., Kocsis, B., Lyra, W., Winter, L. M., 2014, MNRAS, 441, 900
Montuori, C., Dotti, M., Colpi, P., Decarli, R., Haart, F., 2011, MNRAS, 412, 26
Montuori, C., Dotti, M,. Haardt, F., Colpi, M., Decarli, R., 2012, MNRAS, 425, 1633
Nixon, C. J., King, A. R., Pringle, J. E., 2011, MNRAS, 417, L66
Nixon, C. J., Cossins, P. J., King, A. R., Pringle, J. E., 2011, MNRAS, 412, 1591
Ogilvie, G. I., 1999, MNRAS, 304, 557
Paardekooper, S.-J., Papaloizou, J. C. B., 2009, MNRAS, 394, 2297
Papaloizou, J., Lin, D. N. C., 1984, ApJ, 285, 818
Papaloizou, J. C. B., Terquem, C., 2001, MNRAS, 325, 221
Papaloizou, J. C. B., Terquem, C., 2006, Reports on Progress in Physics, 69, 119
Podlewska-Gaca E., Papaloizou, J. C. B., Szuszkiewicz, E., 2012, MNRAS, 421, 1736
Polnarev A. G., Rees, M. J., 1994, A&A, 283, 301
Rafikov, R., 2013, ApJ, 774, 144
Rasio, F. A., Ford, E. R., 1996, Science, 274, 954
Rieger, F. M., Mannheim, K., 2000, A&A 359, 948
Roedig, C., Sesana, A., Dotti, M., Cuadra, J., Amaro-Seoane, P., Haart, F., 2012, A&A, 545, 127
Roedig, C. , Krolik, J., Miller, M., 2014, ApJ, 785, 115
Roedig, C., Sesana, A., 2014, MNRAS, 439, 3476
Rossi, E. M., Lodato, G., Armitage, P. J., Pringle, J. E., King, A. R., 2010, MNRAS, 401, 2021
Scheuer, P. A. G., Feiler, R., 1996, MNRAS. 282, 291
Sesana, A., Roedig, C., Reynolds, M., Dotti, M., 2012, MNRAS, 420, 860
Shakura, N. I., 1973, Soviet Astronomy, 16, 756
Shakura, N. I., Sunyaev, R. A., 1973, A&A, 24, 337
Shapiro, S. L., 2010, Phys. Rev. D., 81, 4019
Sorathia, K. A., Krolik, J. H., Hawley, J. F. 2013, ApJ, 768, 133
Tanaka, H., Takeuchi, T., Ward, W. R., 2002, ApJ, 565, 1257
Tanaka, T., Menou, K., Haiman, Z., 2012, MNRAS, 420, 705
Thakar, A. R., Ryden, B. S., 1998, ApJ, 506, 93
Valtonen, M. J., Ciprini, S., Lehto, H. J., 2012, MNRAS, 427, 77
Yu, Q., Lu, Y., 2001, A&A, 377, 17
Ziglin, S. L., 1975, Soviet Astronomy Letters, 1, 194

Appendix A: The evolution of a finite disk with $a = b = 0$

When $a = b = 0$ equation (63) becomes a linear equation taking on the simple form

$$\frac{\partial\tilde{\Phi}}{\partial\tau} = \frac{1}{h^2}\frac{\partial^2\tilde{\Phi}}{\partial h^2}, \qquad (A.1)$$

where $\tilde{\Phi} = h\tilde{\Sigma}$. We express the solution of (A.1) for $h \in (1, h_{out})$ as a linear combination of normal modes in the form

$$\tilde{\Phi} = \sum_i a_i\phi_i(h)e^{-\lambda_i\tau}. \qquad (A.2)$$

The boundary conditions satisfied by $\Phi(h,\tau)$ (and also $\phi_i(h), i = 1, 2...$) are

$$\tilde{\Phi}(h=1) = 0, \quad \text{and} \quad \frac{\partial\Phi(h=h_{out})}{\partial h} = 0. \qquad (A.3)$$

The required solution to (A.2) should also satisfy the initial condition $\Phi(\tau = 0) = 1$.

Let recall that in order to express the surface density in physical units, we must multiply $\tilde{\Sigma}$ by product of a numerical factor and M/r_p^2, where the numerical factor is determined by the specification of the ratio of the disk mass to the mass of the central body within the computational domain. For the particular numerical simulations discussed in this Paper, the numerical factor relating the quantity $\Phi = \Sigma/\sqrt{GMr_p}$ to $\tilde{\Phi}$, Φ_0, is approximately equal to $2.4\cdot10^{-4}$. Note, however, that the initial condition is incompatible with the inner boundary condition (A.3). This is due to the fact that our boundary conditions are strictly valid only after some period of time has elapsed. Nonetheless, the choice of the functions $\phi_i(h)$ enables the initial condition to be satisfied everywhere apart from at $h = 1$, see below. After substitution of (A.2) to (A.1) we get

$$\frac{d^2\phi_i}{dh^2} + \lambda_i h^2\phi_i = 0. \qquad (A.4)$$

Note that the solutions to (A.4) are orthogonal with respect to the scalar product

$$< \phi_i|\phi_j >= \int_1^{h_{out}} dh h^2\phi_i\phi_j. \qquad (A.5)$$

They can be expressed in terms of Bessel functions as

$$\phi_i = \sqrt{h}(C_1 J_{1/4}(z) + C_2 J_{-1/4}(z)), \qquad (A.6)$$

where $z = \lambda_i h^2/2$. The boundary conditions (A.3) then define an eigenvalue problem leading to a discrete set of positive λ_i bounded from below. We arrange the eigenvalues in such a way that larger eigenvalues correspond to larger values of i, and calculate them numerically for $i = 0, 1, ..13$, with $i = 0$ corresponding to the mode with the smallest value of λ for a given h_{out}. The dependence λ_0 on h_{out} is shown in Fig. A.1.

When $\lambda_i \gg 1$ we can use the asymptotic representation of the Bessel functions corresponding to large values of their arguments. In this case it is easy to show that λ_i approximately satisfy

$$\lambda_i \approx \pi^2\left(\frac{1+2i}{h_{out}^2-1}\right)^2. \qquad (A.7)$$

We have checked that the approximate values (A.7) are close to the ones obtained numerically even for $i = 1$.

In order to find the coefficients a_i in (A.2) we use the formal identity $1 = \sum_i a_i\phi_i(h)$ and the orthogonality condition (A.5) to get

$$a_i = \frac{I_2}{I_1}, \quad \text{with} \quad I_1 = \int_1^{h_{out}} dh h^2\phi_i(h)^2 \quad \text{and}$$
$$I_2 = \int_1^{h_{out}} dh h^2\phi_i(h) = \frac{1}{\lambda_i}\frac{d}{dh}\phi_i(h=1), \qquad (A.8)$$

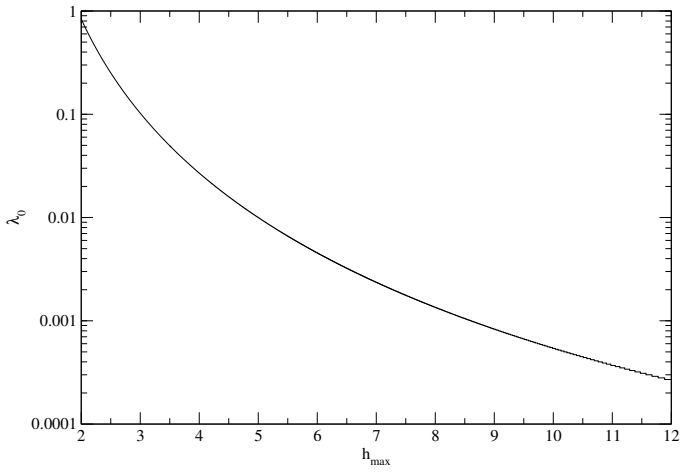

Fig. A.1. The minimum eigenvalue λ_0 as a function of the outer boundary location of the computational domain.

where we have used equation (A.4) to obtain the last equality.

For our purposes we need to know the value of the quantity $F_- \equiv \partial\tilde{\Phi}/\partial h$, evaluated at $h = 1$. It is easy to see that this can be represented in the form

$$F_- = \sum_i \lambda_i \Psi_i e^{-\lambda_i \tau}, \quad \text{with} \quad \Psi_i = \frac{a_i}{\lambda_i}\frac{d}{dh}\phi_i(h=1). \tag{A.9}$$

In general the coefficients Ψ_i have to be be calculated numerically. Thus we obtain $\Psi_0 = 3.1$. For large values of i the asymptotic representation of the Bessel functions may be used, as for eigenvalue determination, with the result

$$\Psi_i \approx \frac{4}{\lambda_i(h_{out}^2 - 1)}, \tag{A.10}$$

where we can use equation (A.7) to specify λ_i. Note that equation (A.10) is found to give reasonable values for Ψ_i even when i is small. Thus for $i = 1$ the numerical value of $\Psi_1 \approx 0.2$, whereas equation (A.10) gives $\Psi_1 \approx 0.18$.

A.1. Orbital evolution

Now let us consider the orbital evolution. In order to find the dependence of r_p on time we again use equations (6), (7) and (62) recalling that the relationship between the mass flux $\dot{M}$ and the quantity F_- as given by $\dot{M} = \dot{M}_* F_- = 3\pi\nu_0\Sigma_0 F_-$ (see equation (36) and preceding discussion). We take account of the effect of evolution of perturber's orbital distance r_p with time, on the surface density profile, in the simplest possible manner, by utilising an appropriate scaling of quantities of interest with the ratio r_p/r_0 as in the main text. We recall that since the inner boundary condition in (A.3) assumes that the variable h is always equal to unity at the perturber's position it is convenient to redefine this quantity according to $h = \sqrt{r/r_p}$, which strictly coincides with the older definition only when $t = 0$. Furthermore, we redefine the dimensionless time τ assuming that in equation (35) r_p replaces r_0. Thus we have $\tau = 3\nu_0 t/r_p^2$. However, the definition of the dimensionless surface density $\tilde{\Sigma}$ and the relation between ν and Σ given by equation (33) remain unchanged.

We proceed by introducing the dimensionless time variable $\tilde{t} = t/P_0$, where $P_0 = 2\pi r_0^{3/2}/\sqrt{GM}$ and the dimensionless orbital distance $\tilde{r}_p = r_p/r_0$. Utilising equations (6), (7) and (62), it is straightforward to obtain an equation governing the orbital evolution in terms of these quantities. This takes the form

$$\frac{1}{\tilde{r}_p}\frac{d\tilde{r}_p}{d\tilde{t}} = -\frac{12\pi^2}{q}\nu_*\Sigma_* F_-, \tag{A.11}$$

where $\Sigma_* = r_0^2\Sigma_0/M$ and $\nu_* = \nu_0/\sqrt{GMr_0}$. For the simulation discussed above, $\Sigma_* \approx 2.4 \cdot 10^{-4}$ and $\nu_* = 10^{-5}$.

From equation (A.9) it follow that F_- can be written in the form

$$F_- = \sum_i \lambda_i \Psi_i e^{-\Lambda_i \tilde{t}} \quad \text{with} \quad \Lambda_i = \frac{3\pi}{2\tilde{r}_p^2}\nu_*\lambda_i. \tag{A.12}$$

We integrate (A.12) formally assuming that r_p does not depend on time on the r.h.s. to obtain

$$\tilde{r}_p = e^{-\Delta}, \quad \Delta = \frac{8\pi\tilde{r}_p^2}{q}\Sigma_* \sum_i \Psi_i(1 - e^{-\Lambda_i\tilde{t}}). \tag{A.13}$$

Note that equation (A.13) provides an implicit dependence of $\tilde{r}_p$ on time since $\tilde{r}_p$ enters both sides of the equation. Its numerical solution by a standard iterative procedure is shown in Fig. 16.